

Improving 3D Cellular Positioning Integrity with Bayesian RAIM

Liqin Ding, *Member, IEEE*, Gonzalo Seco-Granados, *Fellow, IEEE*, Hyowon Kim, *Member, IEEE*, Russ Whiton, Erik G. Ström, *Fellow, IEEE* Jonas Sjöberg, Henk Wymeersch *Fellow, IEEE*

Abstract—Ensuring positioning integrity amid faulty measurements is crucial for safety-critical applications, making receiver autonomous integrity monitoring (RAIM) indispensable. This paper introduces a Bayesian RAIM algorithm with a streamlined architecture for snapshot-type 3D cellular positioning. Unlike traditional frequentist-type RAIM algorithms, it computes the exact posterior probability density function (PDF) of the position vector as a Gaussian mixture (GM) model using efficient message passing along a factor graph. This Bayesian approach retains all crucial information from the measurements, eliminates the need to discard faulty measurements, and results in tighter protection levels (PLs) in 3D space and 1D/2D subspaces that meet target integrity risk (TIR) requirements. Numerical simulations demonstrate that the Bayesian RAIM algorithm significantly outperforms a baseline algorithm, achieving over 50% PL reduction at a comparable computational cost.

I. INTRODUCTION

The advent of cellular networks brings promising enhancements in reliable positioning services, which are essential for applications like factory automation and autonomous driving [2], [3]. These sectors demand not only high accuracy and low latency but also stringent positioning *integrity* to ensure trustworthiness for downstream applications [4], [5]. While accuracy measures the closeness of the estimated position of a user equipment (UE) to its true position over a longer period and under nominal conditions, integrity assesses the real-time reliability of positioning estimates in the potential presence of measurement faults [6]. According to 3GPP, integrity guarantees for standalone radio positioning will be introduced in Release-18 and beyond [7], [8]. In this evolving landscape, receiver autonomous integrity monitoring (RAIM) [6], [9] is expected to play a crucial role.

Originally developed for global navigation satellite systems (GNSS) to meet the aviation industry’s stringent safety requirements [10]–[15], RAIM has been adapted for various safety-critical positioning and navigation systems [6], [9], [16]–[18]. RAIM’s primary goal is to eliminate the effects of faulty measurements to achieve an accurate position estimate,

and to compute an upper bound on the instantaneous position error, known as the protection level (PL). The PL ensures that the probability of the true position error exceeding this bound is less than the target integrity risk (TIR), thus quantifying integrity at a specified confidence level [6]. Traditional RAIM schemes achieve this through two steps: fault detection and exclusion (FDE) and error bounding. They rely on measurement redundancy and perform consistency checks either in the measurement domain (e.g., comparing measurement residuals [10]–[13]) or in the position domain (e.g., using solution separation (SS) testing [14]) for FDE. These methods, which are frequentist in nature, tend to produce conservative PLs and thus lead to reduced availability [6].

The Bayesian RAIM framework, proposed relatively recently [19], [20], offers a robust alternative by assessing integrity based on the posterior probability distribution of the UE position, integrating all prior information and current measurements. Current research on Bayesian RAIM is limited, with most approaches relying on Monte Carlo methods such as particle filters [20]–[22] or Gibbs samplers [23] to approximate the posterior distribution. These methods, while powerful, can be computationally demanding and may not scale well with increased system complexity. In our prior work [1], we alternatively developed a Bayesian RAIM algorithm for time-of-arrival (ToA)-based cellular positioning in a simplified 1D setting using efficient message passing along a factor graph. The computed PLs are proven to be significantly tighter compared to traditional RAIM [14].

In this paper, we extend previous developments [1] to 3D positioning, addressing challenges in message passing and precise PL computation. Specifically, we focus on (i) accurately computing the weights of the GM models (ignored in [24], [25]), (ii) efficiently handling degenerate Gaussian densities in message passing; and (iii) precisely assessing the probability of a Gaussian distributed random vector within an arbitrary sphere in \mathbb{R}^n for $n \geq 2$ for PL computation. Our main contributions are:

- **Explicit Message Passing Rules for Degenerate Densities:** We introduce efficient computational rules for Gaussian message passing to ensure precise scaling factor calculations for multiple lower-dimensional measurements of a random vector via linear mapping, including rules for the inverse of linear mappings and the product of multiple, potentially degenerate, Gaussian densities.
- **Tight 2D/3D PL Computation:** We develop a numerical integration-based method to accurately assess the probability of a Gaussian-distributed random vector residing

This project has been supported in part by the European Union’s Horizon 2020 research and innovation programme under grant agreement No. 101006664, and in part by the Catalan ICREA Academia Program. The authors would like to thank all partners within Hi-Drive for their cooperation and valuable contribution. This paper is extended from [1].

L. Ding, E. G. Ström, J. Sjöberg, and H. Wymeersch are with the Department of Electrical Engineering, Chalmers University of Technology, Gothenburg, Sweden.

G. Seco-Granados is with Department of Telecommunications and Systems Engineering, Universitat Autònoma de Barcelona, Barcelona, Spain.

H. Kim is with the Department of Electronics Engineering, Chungnam National University, Daejeon 34134, South Korea.

R. Whiton is with Volvo Car Corporation, Gothenburg, Sweden.

within an arbitrary ellipsoid in \mathbb{R}^n . This advancement enables precise 2D/3D PL computations based on the probability density function (PDF) of the position, whether in Gaussian or Gaussian mixture (GM) model forms.

- **Performance Evaluation and Comparison:** Using the above methods, we develop a Bayesian RAIM algorithm for 3D positioning. Monte-Carlo simulations show that our algorithm provides significantly tighter PLs compared to a baseline RAIM algorithm adapted from [14], at a comparable computational cost using a PL overestimation method. With the developed precise PL computation method, it achieves further PL reduction, albeit with increased computational complexity.

The paper is organized as follows: Section II details the ToA-based 3D positioning problem and integrity monitoring, including the formal definition of the n -dimensional PL. Section III covers the Baseline RAIM algorithm. Section IV presents the message passing process for the Bayesian RAIM algorithm, and Section V describes the PL computation methods. The numerical study is in Section VI. Finally, conclusions are drawn in Section VII.

Notations: We use uppercase letters like X for random scalars and boldface uppercase letters like $\mathbf{X} = (X_1, \dots, X_n)^T$ for random vectors. Lowercase letters like x denote deterministic scalars, bold lowercase letters like $\mathbf{x} = (x_1, \dots, x_n)^T$ denote deterministic vectors, and uppercase sans-serif letters like A denote deterministic matrices. We write $A \succeq 0$ and $A \succ 0$ for symmetric positive semidefinite and definite matrices, respectively. $\mathbf{X} \sim \mathcal{N}(\mathbf{x}; \mathbf{m}, \Sigma)$ indicates that \mathbf{X} is a Gaussian vector with mean \mathbf{m} and covariance $\Sigma \succeq 0$, and $X \sim \mathcal{N}(x; m, \sigma^2)$ indicates that X is a Gaussian variable with mean m and variance σ^2 .

II. PROBLEM FORMULATION

A. System Model and Assumptions

We consider a single epoch of the positioning problem with M time-synchronized base stations (BSs) collaborating in downlink positioning of a UE. The UE's four unknowns include its 3D position $\mathbf{x}_u = (x_{u,1}, x_{u,2}, x_{u,3})^T \in \mathbb{R}^3$ in the network coordinate reference system and its clock bias $x_c \in \mathbb{R}$. The positions of the M BSs are known and expressed as $\mathbf{x}_i = (x_{i,1}, x_{i,2}, x_{i,3})^T \in \mathbb{R}^3$ for $i = 1, \dots, M$. The BSs send coordinated positioning reference signals (PRSs) to the UE to estimate M ToAs for the line-of-sight (LoS) paths. These ToAs convert to pseudoranges as $d_i = \|\mathbf{x}_i - \mathbf{x}_u\| + x_c + b_i + n_i$, $i = 1, \dots, M$, where n_i is measurement noise, and b_i represents measurement bias caused by faults.

As usually assumed, an initial position estimate $\mathbf{x}_{u,0}$ is available. Linearizing $\|\mathbf{x}_i - \mathbf{x}_u\|$ around $\mathbf{x}_{u,0}$ using a first-order Taylor expansion yields [26]–[28]

$$d_i \approx \|\mathbf{x}_i - \mathbf{x}_{u,0}\| + \mathbf{g}_i^T (\mathbf{x}_u - \mathbf{x}_{u,0}) + x_c + b_i + n_i, \quad (1)$$

where $\mathbf{g}_i \triangleq (\mathbf{x}_{u,0} - \mathbf{x}_i) / \|\mathbf{x}_{u,0} - \mathbf{x}_i\|$ is the unit vector from $\mathbf{x}_{u,0}$ to \mathbf{x}_i . Letting $\mathbf{h}_i = [\mathbf{g}_i^T \ 1]^T$ and $\mathbf{x} = [\mathbf{x}_u^T \ x_c]^T$, we establish a linear measurement model

$$y_i = \mathbf{h}_i^T \mathbf{x} + b_i + n_i, \quad i = 1, \dots, M, \quad (2)$$

which serves as an approximation to $d_i - \|\mathbf{x}_i - \mathbf{x}_{u,0}\| + \mathbf{g}_i^T \mathbf{x}_{u,0}$. Arranging the M row vectors \mathbf{h}_i^T into an $M \times 4$ matrix \mathbf{H} and

forming y_i , b_i , and n_i into length- M column vectors \mathbf{y} , \mathbf{b} , and \mathbf{n} , the model can be expressed in matrix form

$$\mathbf{y} = \mathbf{H}\mathbf{x} + \mathbf{b} + \mathbf{n}. \quad (3)$$

The initial position estimate error $\mathbf{e}_0 \triangleq \mathbf{x}_u - \mathbf{x}_{u,0}$ introduces approximation errors through the approximation (1), affecting the performance of any method that relies on this model.

We treat $\mathbf{x} \in \mathbb{R}^4$, b_i and n_i as realizations of the random vector/variable $\mathbf{X} = [X_1, X_2, X_3, X_4]^T$, B_i and N_i , respectively. To indicate the measurement state of y_i , we introduce a latent random variable Λ_i with realization λ_i , which follows the Bernoulli probability mass function (PMF) $p_{\Lambda_i}(\lambda_i) = \theta_i^{\lambda_i} (1 - \theta_i)^{(1-\lambda_i)}$ where $0 < \theta_i \ll 1$. The value $\Lambda_i = 0$ denotes a fault-free measurement with $B_i \sim \mathcal{N}(0, 0)$, and $\Lambda_i = 1$ indicates a faulty measurement with $B_i \sim \mathcal{N}(m_{b,i}, \sigma_{b,i}^2)$. Measurement noises are zero-mean Gaussian: $N_i \sim \mathcal{N}(0, \sigma_{n,i}^2)$. The random variables $\{\Lambda_i\}$, $\{B_i\}$ and $\{N_i\}$ are considered independent within each set. The fault probability θ_i , derived from previous system operations, is assumed to be known.

B. n -Dimensional Protection Level

To measure the integrity of positioning results, PLs are computed under the specified TIR requirements. In the context of 3D positioning, PLs can be determined for the full 3D space and its 1D or 2D subspaces. We define n -dimensional PL ($n = 1, 2, 3$) using the 3D positioning error vector $\mathbf{e}_{3D} \triangleq \mathbf{x}_u - \hat{\mathbf{x}}_u \in \mathbb{R}^3$, where $\hat{\mathbf{x}}_u \triangleq \hat{\mathbf{x}}_{1:3}$ is the position estimate. Consider two orthogonal unit vectors $\tilde{\mathbf{v}}_1, \tilde{\mathbf{v}}_2 \in \mathbb{R}^3$. The 1D subspace spanned by $\tilde{\mathbf{v}}_1$ is $\mathcal{L}(\tilde{\mathbf{v}}_1) \triangleq \{s\tilde{\mathbf{v}}_1 \mid s \in \mathbb{R}\}$, and the 2D subspace spanned by both vectors is $\mathcal{P}(\tilde{\mathbf{v}}_1, \tilde{\mathbf{v}}_2) \triangleq \{s\tilde{\mathbf{v}}_1 + t\tilde{\mathbf{v}}_2 \mid s, t \in \mathbb{R}\}$. The projections of \mathbf{e}_{3D} onto these subspaces are $\mathbf{e}_{1D} = \tilde{\mathbf{v}}_1^T \mathbf{e}_{3D}$ and $\mathbf{e}_{2D} = (\tilde{\mathbf{v}}_1^T \mathbf{e}_{3D}, \tilde{\mathbf{v}}_2^T \mathbf{e}_{3D})^T$.

Definition 1. The n -dimensional PL for the position estimate $\hat{\mathbf{x}}_u$ in $\mathcal{L}(\tilde{\mathbf{v}}_1)$ ($n = 1$), $\mathcal{P}(\tilde{\mathbf{v}}_1, \tilde{\mathbf{v}}_2)$ ($n = 2$), or \mathbb{R}^3 ($n = 3$), for a TIR of P_{TIR} , is the minimum distance r such that the actual integrity risk (IR), $\Pr\{\|\mathbf{e}_{nD}\| > r\}$, does not exceed P_{TIR}

$$\text{PL}_{nD}(P_{\text{TIR}}) = \min\{r \mid \Pr\{\|\mathbf{e}_{nD}\| > r\} < P_{\text{TIR}}\}. \quad (4)$$

Geometrically, $\text{PL}_{nD}(P_{\text{TIR}})$ is the radius of the smallest interval, circle, or sphere centered on the estimated position that encompasses \mathbf{e}_{nD} with a probability of at least $1 - P_{\text{TIR}}$. For $n = 2$ or 3 , $\text{PL}_{nD}(P_{\text{TIR}})$ bounds \mathbf{e}_{nD} in any direction within the specified n -dimensional space. If the actual IR for a given r can be precisely or approximately computed for 1D subspaces, an overestimate of the 2D/3D PL can be determined using the following lemma.

Lemma 1. For $n = 2$ or 3 , given $\mathbf{e}_{nD} = (e_1, \dots, e_n)^T$ and weights¹ $\{w_1, \dots, w_n\}$ such that $0 < w_i < 1$ for all i and $\sum_{i=1}^n w_i = 1$, if $\{\text{PL}_{1D,1}, \dots, \text{PL}_{1D,n}\}$ are obtained such that

$$\text{PL}_{1D,i} = \min\{r \mid \Pr\{|e_i| > r\} < w_i P_{\text{TIR}}\}, \quad (5)$$

then $\Pr\{\|\mathbf{e}_{nD}\| > \text{PL}_{nD}^U\} < P_{\text{TIR}}$ can be guaranteed, where

$$\text{PL}_{nD}^U = \left(\sum_{i=1}^n \text{PL}_{1D,i}^2 \right)^{1/2}. \quad (6)$$

¹Choosing $w_i = 1/n$ for all i is pragmatic when positioning error distributions are similar across coordinate directions. Adjusting these weights can refine the overestimate, leading to tighter results. Conversely, setting w_i close to 0 can significantly increase $\text{PL}_{1D,i}$ and consequently enlarge PL_{nD}^U .

Proof. See Appendix A. \square

Example 1. Fig. 1 shows a scenario where the UE is equipped in a vehicle on a curved road in the horizontal-plane (x - y plane). To ensure the vehicle remains within its lane, the position error perpendicular to the road ($\tilde{\mathbf{v}}_{\perp}$ direction) needs to stay within a margin at a confidence level of $1 - P_{\text{TIR}}$. As the vehicle navigates the curve, $\tilde{\mathbf{v}}_{\perp}$ changes. If $\tilde{\mathbf{v}}_{\perp}$ is known in real-time, the positioning system can compute $\text{PL}_{1\text{D}}$ (P_{TIR}) for $\mathcal{L}(\tilde{\mathbf{v}}_{\perp})$. Otherwise, it can provide an overestimated 2D PL $\text{PL}_{2\text{D}}^U = (\text{PL}_{1\text{D},1}^2 + \text{PL}_{1\text{D},2}^2)^{1/2}$, where $\text{PL}_{1\text{D},1}$ and $\text{PL}_{1\text{D},2}$ are 1D PLs computed for $\tilde{\mathbf{v}}_1 = (1, 0, 0)^T$ and $\tilde{\mathbf{v}}_2 = (0, 1, 0)^T$, with $w_1 = w_2 = 0.5$. It is conceivable that by slightly decreasing w_1 and increasing w_2 , the blue rectangle can become closer to a square, resulting in a tighter overestimate.

PL requirements vary by application and must align with specific operational demands, see e.g. [9, Table II]. In Fig. 1, $\text{PL}_{2\text{D}}^U$ might suffice for placing a vehicle on the correct road, suitable for automatic tolling, but it cannot ensure accurate lane positioning, which is crucial for automated driving.

III. BASELINE RAIM ALGORITHM

To benchmark performance, we adapt the advanced RAIM algorithm from [14]. We refer to the adapted algorithm as the *Baseline RAIM²* algorithm. It uses a hypothesis testing framework for FDE. The following inputs are required: $P_{\text{TIR,H}}$ and $P_{\text{TIR,V}}$, the TIR requirements for the horizontal-plane and the vertical direction, and $P_{\text{FA,H}}$ and $P_{\text{FA,V}}$, the respective false alarm budgets. A false alarm occurs if the algorithm detects faults in fault-free measurements. The outputs include a position estimate and PLs for both horizontal and vertical subspaces. The main steps of Baseline RAIM are as follows.

- 1) **Fault mode determination:** Identify a set of *fault modes* (hypotheses) for monitoring, where each fault mode assumes a subset of measurements is faulty and the rest are fault-free. These fault modes are exclusive, meaning only one can occur.
- 2) **SS test for fault detection:** Compute an SS test statistic for each fault mode and position coordinate to evaluate the closeness of different position estimates obtained from assumed fault-free measurements by the fault modes.
- 3) **Fault exclusion (if SS test fails):** If the SS test fails, attempt fault exclusion by repeatedly applying fault detection to subsets of assumed fault-free measurements for each fault mode, starting with the one with the highest probability of occurrence (see Remark 1).
- 4) **Position estimate and PL calculation:** If fault exclusion is successful or not needed, calculate a position estimate and compute two PLs following [14]: one for the horizontal plane and one for the vertical direction.

In this process, the following components are involved: (i) all-in-view position estimation; (ii) fault mode identification; (iii) SS testing; and (iv) PL computations. The following sections provide detailed explanations of these components.

²The dropped term ‘‘advanced’’ emphasizes its ability to detect and exclude multiple faults, which is more advanced than the earliest RAIM algorithm (which could handle only one fault).

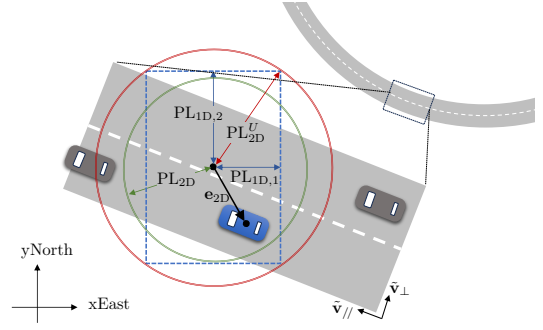


Fig. 1. Illustration of 2D PL computation on the horizontal plane.

A. All-in-View Position Estimation

The all-in-view position assumes all measurements are fault-free. In the linear model (3), when $\mathbf{b} = \mathbf{0}$ and \mathbf{n} follows $\mathcal{N}(\mathbf{0}, \Sigma)$, where Σ is the diagonal covariance matrix with elements $\Sigma_{i,i} = \sigma_{n,i}^2$, $i = 1, \dots, M$, the weighted least squares (WLS) estimate of \mathbf{x} , also the maximum likelihood (ML) estimate under the fault-free assumption, is given by

$$\hat{\mathbf{x}}^{(0)} = (\mathbf{H}^T \Sigma^{-1} \mathbf{H})^{-1} \mathbf{H}^T \Sigma^{-1} \mathbf{y} = \mathbf{A}^{(0)} \mathbf{y}, \quad (7)$$

where $\mathbf{A}^{(0)} \triangleq (\mathbf{H}^T \Sigma^{-1} \mathbf{H})^{-1} \mathbf{H}^T \Sigma^{-1}$. The positioning error vector $\mathbf{x} - \hat{\mathbf{x}}^{(0)} = \mathbf{A}^{(0)} \mathbf{n}$ follows a zero-mean Gaussian distribution with covariance matrix $\Phi^{(0)} \triangleq (\mathbf{H}^T \Sigma^{-1} \mathbf{H})^{-1}$.

B. Fault Modes Identification

To enable SS testing for fault exclusion, an eligible fault mode must contain at least 5 assumed fault-free measurements. Baseline RAIM monitors all eligible modes for optimal performance. The total number of monitored fault modes (with at least one fault) is given by $N_{\text{FM}} = \sum_{j=1}^{M-5} \binom{M}{j}$. For fault mode $k = 1, \dots, N_{\text{FM}}$, let \mathcal{I}_k represent the index set of assumed fault-free measurements, and $\mathcal{I}_k^c \triangleq \{1, 2, \dots, M\} \setminus \mathcal{I}_k$ represent the index set of faulty measurements. The probability of occurrence of fault mode k is $p_{\text{FM},k} = \prod_{i \in \mathcal{I}_k^c} (1 - \theta_i) \prod_{i \in \mathcal{I}_k} \theta_i$. For convenience, we assume that fault modes are sorted in decreasing order of probability of occurrence, thus $p_{\text{FM},k} \geq p_{\text{FM},k+1}$, for $1 \leq k < N_{\text{FM}}$.

C. Solution Separation Testing

For fault mode k , define Σ_k as the diagonal matrix derived from Σ in the following way

$$[\Sigma_k^{-1}]_{i,i} = \begin{cases} 0, & i \in \mathcal{I}_k^c, \\ 1/\sigma_{n,i}^2, & i \in \mathcal{I}_k. \end{cases} \quad (8)$$

The WLS estimate of \mathbf{x} using measurements indexed by \mathcal{I}_k is

$$\hat{\mathbf{x}}^{(k)} = \mathbf{A}^{(k)} \mathbf{y} \quad (9)$$

where $\mathbf{A}^{(k)} \triangleq (\mathbf{H}^T \Sigma_k^{-1} \mathbf{H})^{-1} \mathbf{H}^T \Sigma_k^{-1}$. If all these measurements are fault-free, the positioning error $\mathbf{x} - \hat{\mathbf{x}}^{(k)} = \mathbf{A}^{(k)} \mathbf{n}$ follows a zero-mean Gaussian distribution with covariance matrix $\Phi^{(k)} \triangleq (\mathbf{H}^T \Sigma_k^{-1} \mathbf{H})^{-1}$, and difference between the all-in-view and fault mode k estimates

$$\Delta \hat{\mathbf{x}}^{(k)} \triangleq \hat{\mathbf{x}}^{(0)} - \hat{\mathbf{x}}^{(k)} \quad (10)$$

follows a zero-mean Gaussian distribution with covariance matrix given by $(\mathbf{A}^{(k)} - \mathbf{A}^{(0)}) \Sigma (\mathbf{A}^{(k)} - \mathbf{A}^{(0)})^T$. The SS test statistics used by the Baseline RAIM algorithm are

$$\tau_{n,k} \triangleq |\Delta \hat{\mathbf{x}}_n^{(k)}|, \quad n = 1, 2, 3, \quad k = 1, \dots, N_{\text{FM}}. \quad (11)$$

The SS test compares $\tau_{n,k}$ with a test threshold $T_{n,k}$ for each position coordinate and fault mode. Only if $\tau_{n,k} \leq T_{n,k}$ for all $n = 1, 2, 3$ and $k = 1, \dots, N_{\text{FM}}$, are the M measurements considered fault-free, and the algorithm outputs $\hat{\mathbf{x}}_{\text{u}} = \hat{\mathbf{x}}_{1:3}^{(0)}$ as the 3D position estimate. If $\tau_{n,k} > T_{n,k}$ for any n, k , the algorithm proceeds to fault exclusion. The test thresholds are determined based on the false alarm budgets $P_{\text{FA,H}}$ and $P_{\text{FA,V}}$ ³. The algorithm distributes $P_{\text{FA,H}}$ evenly between the two horizontal position coordinates x_1 and x_2 , and then distributes each coordinate's false alarm budget evenly across the N_{FM} fault modes. For $k = 1, \dots, N_{\text{FM}}$, the thresholds are

$$T_{n,k} = \begin{cases} \sigma_{ss,n}^{(k)} Q^{-1} \left(\frac{P_{\text{FA,H}}}{4N_{\text{FM}}} \right), & n = 1, 2 \\ \sigma_{ss,n}^{(k)} Q^{-1} \left(\frac{P_{\text{FA,V}}}{2N_{\text{FM}}} \right), & n = 3 \end{cases} \quad (12)$$

where $\sigma_{ss,n}^{(k)} \triangleq [(A^{(k)} - A^{(0)})\Sigma(A^{(k)} - A^{(0)})^T]_{n,n}^{1/2}$, and $Q^{-1}(\cdot)$ is the inverse of the Q function: $Q(u) = \frac{1}{\sqrt{2\pi}} \int_u^{+\infty} e^{-\frac{t^2}{2}} dt$.

Remark 1 (Fault exclusion process). When the SS test fails, the algorithm attempts to exclude the faulty measurements by reapplying the fault mode identification and SS testing to subsets of assumed fault-free measurements specified by the N_{FM} fault modes, ordered by decreasing probability of occurrence. This continues until the SS test passes or all fault modes are checked, indicating fault exclusion failure. Upon reaching fault mode k in this process, the subset of measurements indexed by \mathcal{I}_k are checked, and a new list of $N_{\text{FM},k} = \sum_{j=1}^{|\mathcal{I}_k|-5} \binom{|\mathcal{I}_k|}{j}$ fault modes is identified. If the SS testing is successful, fault mode k is considered true, and the algorithm returns the position estimate ($\hat{\mathbf{x}}_{\text{u}} = \hat{\mathbf{x}}_{1:3}^{(k)}$) and PLs computed using these $|\mathcal{I}_k|$ measurements. If fault exclusion fails, the algorithm declares that the system cannot provide reliable positioning results (system unavailable).

D. Protection Level Computation

The Baseline RAIM algorithm can compute 1D PLs for each of the three coordinate directions. It can also obtain PL overestimates in the three coordinate planes and the full 3D space using Lemma 1. Below we summarize the formulation of the 1D PL for the vertical direction and the 2D PL overestimate for the horizontal plane as described in [14]. Assume that the SS test passes for the M measurements, so $\hat{\mathbf{x}}_{\text{u}} = \hat{\mathbf{x}}_{1:3}^{(0)}$, and we define $\sigma_n^{(k)} \triangleq [\Phi^{(k)}]_{n,n}^{1/2}$ for $n = 1, 2, 3$ and $k = 0, 1, \dots, N_{\text{FM}}$.

In the vertical direction, the actual IR associated with an arbitrary r is given by $\Pr\{|x_3 - \hat{x}_3^{(0)}| > r\}$. An overbound of the vertical PL PL_V is given by the minimum r satisfying the following condition

$$2Q \left(\frac{r}{\sigma_3^{(0)}} \right) + \sum_{k=1}^{N_{\text{FM}}} p_{\text{FM},k} Q \left(\frac{r - T_{3,k}}{\sigma_3^{(k)}} \right) < P_{\text{TIR,V}}. \quad (13)$$

A bisection search is used to find the smallest r within a given error tolerance r_{tol} . The detailed formulation process can be

³Reducing $P_{\text{FA,H}}$ and $P_{\text{FA,V}}$ increases the test thresholds computed by (12), thus lowering the likelihood of issuing warning for potential faults. This reduces computational costs but raises the risk of misdetection. Conversely, higher $P_{\text{FA,H}}$ and $P_{\text{FA,V}}$ trigger more fault exclusion attempts, raising computational costs but enhancing positioning quality.

found in [14, Appendix H]. In the horizontal plane, $P_{\text{TIR,H}}$ is evenly divided for the x and y directions (i.e., $w_1 = w_2 = 0.5$ in (5)). For $n = 1, 2$, an overbound of the PL PL_n is given by the minimum r_n that satisfies

$$2Q \left(\frac{r_n}{\sigma_n^{(0)}} \right) + \sum_{k=1}^{N_{\text{FM}}} p_{\text{FM},k} Q \left(\frac{r_n - T_{n,k}}{\sigma_n^{(k)}} \right) < \frac{P_{\text{TIR,H}}}{2}. \quad (14)$$

Again, bisection search is used to find these minimum values within error tolerance r_{tol} . Following (6), the horizontal PL overestimate is given by $\text{PL}_H = (\text{PL}_1^2 + \text{PL}_2^2)^{1/2}$.

If the SS test fails for the M measurements and the k th fault mode is accepted during the fault exclusion process, then $\hat{\mathbf{x}}_{\text{u}} = \hat{\mathbf{x}}_{1:3}^{(k)}$, and in (13) and (14), $p_{\text{FM},k}$, $T_{n,k}$, and $\sigma_n^{(k)}$ should be replaced with their counterparts computed for the $N_{\text{FM},k}$ new fault modes. The left-hand sides of (13) and (14) are loose upper bounds of the actual IR related to the 1D positioning error variables [14]. Moreover, PL_H , by formulation, is an overestimate of the 2D PL for the horizontal plane. Due to these, the values obtained for PL_V and PL_H tend to be large. This intrinsic drawback will be addressed by the proposed Bayesian RAIM algorithm.

Remark 2 (Complexity). The Baseline RAIM algorithm has a variable computational complexity due to the varying number of SS tests required (from 1 in the best case and N_{FM} in the worst case). The computational cost of a SS test mainly arises from (7)–(12), which involve matrix operations. The maximum size of the matrices is determined by the number of assumed fault-free measurements in the fault mode under examination, ranging between M and 5. To reduce complexity, fault modes with occurrence probabilities significantly lower than the TIR can be excluded from monitoring [14]. The PL computation using bisection search contributes little to the overall computational cost, which will be evident from numerical study. The bisection search is an iterative algorithm with variable number of iterations, denoted by $N_{\text{it}} > 0$. The complexity is $\mathcal{O}(N_{\text{it}}N_{\text{FM}})$ since both (13) and (14) involve approximately N_{FM} Q -function value computations.

IV. BAYESIAN RAIM PART I: MESSAGE PASSING

The linear Gaussian measurement model (2) allows a precise computation of the posterior probability distribution of \mathbf{X} , the random vector representing 3D position and clock bias, for each positioning epoch. This section details how the proposed Bayesian RAIM algorithm performs this computation through message passing along a factor graph.

A. Factor Graph Construction and Message Passing Schedule

First, we construct a factor graph for the 3D positioning problem. By introducing an auxiliary random variable $\Gamma_i = \mathbf{h}_i^T \mathbf{X}$ for $i = 1, \dots, M$, we write the measurement model (2) as $y_i = \gamma_i + b_i + n_i$, where γ_i is a realization of Γ_i . We form the sets of random variables $\{Y_i\}$, $\{B_i\}$, $\{\Gamma_i\}$, and $\{\Lambda_i\}$ into random vectors \mathbf{Y} , \mathbf{B} , $\mathbf{\Gamma}$, and $\mathbf{\Lambda}$, and their realizations into vectors \mathbf{y} , \mathbf{b} , $\boldsymbol{\gamma}$, and $\boldsymbol{\lambda}$. Following the assumptions in Section II-A, we factorize the joint posterior probability of $\mathbf{\Gamma}$, \mathbf{X} , \mathbf{B} , and $\mathbf{\Lambda}$ as shown in equation (*) in Fig. 2, and form a cycle-free factor graph with M branches to represent the

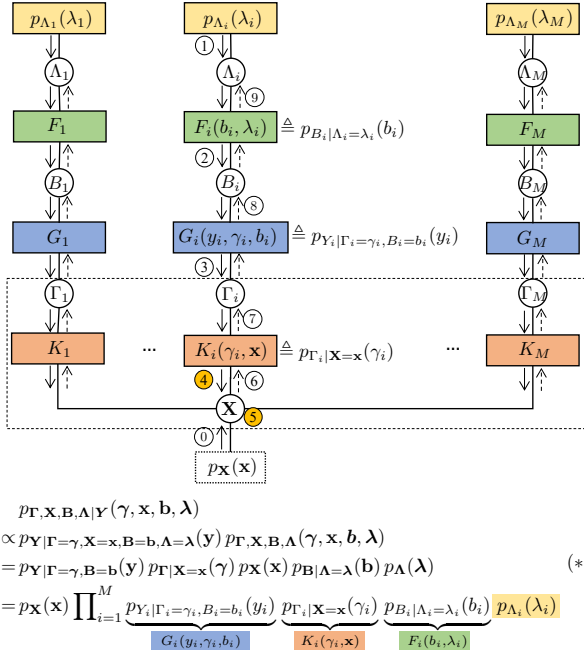


Fig. 2. The factor graph used by the Bayesian RAIM algorithm, constructed according to the joint posterior probability factorization given by (*). The order of message computation and passing is given by the numbers in circles (shown only on the i th branch, but is the same for all branches), while the arrows indicate the passing direction.

factorization, shown in the same figure. Each term in equation (*) corresponds to a factor (function) node in the graph, and for ease of description, we define

$$G_i(y_i, \gamma_i, b_i) \triangleq p_{Y_i | \Gamma_i = \gamma_i, B_i = b_i}(y_i), \quad (15a)$$

$$K_i(\gamma_i, \mathbf{x}) \triangleq p_{\Gamma_i | \mathbf{X} = \mathbf{x}}(\gamma_i) = \delta(\gamma_i - \mathbf{h}_i^T \mathbf{x}), \quad (15b)$$

$$F_i(b_i, \lambda_i) \triangleq p_{B_i | \Lambda_i = \lambda_i}(b_i). \quad (15c)$$

In equation (*), $p_{\mathbf{X}}(\mathbf{x})$ represents the prior PDF of \mathbf{X} . Since we are focusing on a single epoch, we will omit $p_{\mathbf{X}}(\mathbf{x})$ from message passing.

The sum-product rule [29] is adopted for running the message passing on the cycle-free factor graph, and the schedule is straightforward as follows: Messages are passed from variable node Λ_i to variable node \mathbf{X} in steps ①-④ along all M branches. In step ⑤, variable node \mathbf{X} computes the product of all received messages, which after normalization is the posterior PDF of \mathbf{X} . These steps are sufficient for position estimation and PL computation of the current positioning epoch. Optionally, messages can be further passed back to variable node Λ_i in steps ⑥-⑨ along each branch to obtain the posterior PMF of Λ_i .⁴

B. General Gaussian Message Computation Rules

Message computation in steps ④-⑥ is challenging because the messages consist of GM models, i.e. weighted sums of Gaussians. They require precise computation of weights, and the Gaussian densities may be degenerate with rank-deficient covariance matrices. Specifically, step ④ involves inferring

⁴In a real-life positioning system, measurement states in consecutive epochs are likely correlated, making it reasonable to update $p_{\Lambda_i}(\lambda_i)$ for the next positioning epoch using the obtained posterior PMF. However, as this is beyond the scope of this paper, so steps ⑥-⑨ are not discussed further.

a message of \mathbf{X} from a lower-dimensional subspace GM model of Y_i , which yields degenerate Gaussian densities. Steps ⑤ and ⑥ involve computing the product of multiple such messages. Appendix B, rigorously addresses the computational rules for these steps in the following general problem setting.

Problem 1. For $i = 1, \dots, K$, given a linear mapping $\mathbf{Y}_i = \mathbf{A}_i \mathbf{X}$, where $\mathbf{X} \in \mathbb{R}^n$ and $\mathbf{Y}_i \in \mathbb{R}^{m_i}$ are Gaussian random vectors, each matrix $\mathbf{A}_i \in \mathbb{R}^{m_i \times n}$ is full-rank⁵, with $\text{rank}(\mathbf{A}_i) = m_i \leq n$. The objective is to infer the PDF of \mathbf{X} from the known non-degenerate PDF of \mathbf{Y}_i for all i , and then compute the product of all inferred PDFs of \mathbf{X} .

By letting $\mathbf{A}_i = \mathbf{h}_i^T$, our problem becomes a special case of this general problem. A general Gaussian distribution for a random vector $\mathbf{X} \in \mathbb{R}^n$ is characterized by a symmetric positive semi-definite covariance matrix $\boldsymbol{\Sigma} \succeq 0$ and a mean vector $\mathbf{m} \in \mathbb{R}^n$, or equivalently, by $\mathbf{V} \triangleq \boldsymbol{\Sigma}^+$ (the pseudo-inverse of $\boldsymbol{\Sigma}$) and $\mathbf{u} \triangleq \mathbf{V} \mathbf{m}$. Notably, $\text{rank}(\boldsymbol{\Sigma}) = \text{rank}(\mathbf{V}) \leq n$, with the $<$ relation occurring when the distribution is degenerate. The PDF expressed using $(\mathbf{m}, \boldsymbol{\Sigma})$ is denoted $f_{\mathbf{X}}(\mathbf{x}; \mathbf{m}, \boldsymbol{\Sigma})$ (see (43)), and when using (\mathbf{u}, \mathbf{V}) , it is denoted $f_{\mathbf{X}}^{\mathbf{E}}(\mathbf{x}; \mathbf{u}, \mathbf{V})$ (see (45)). Moreover,

$$\alpha_{\mathbf{X}} \triangleq -\frac{1}{2} \mathbf{m}^T \boldsymbol{\Sigma}^+ \mathbf{m} \equiv -\frac{1}{2} \mathbf{u}^T \mathbf{V}^+ \mathbf{u} \quad (16)$$

is defined to simplify expressions. The computation rules are summarized in Lemma 2, Lemma 3, and Remark 3.

Lemma 2 (Inverse of linear mapping). Consider a linear mapping $\mathbf{Y} = \mathbf{A} \mathbf{X}$, where $\mathbf{X} \in \mathbb{R}^n$ and $\mathbf{Y} \in \mathbb{R}^m$ are Gaussian random vectors, $\mathbf{A} \in \mathbb{R}^{m \times n}$, and $\text{rank}(\mathbf{A}) = m \leq n$. Given a message of \mathbf{Y} : $\mu_{\mathbf{Y}}(\mathbf{y}) = f_{\mathbf{Y}}^{\mathbf{E}}(\mathbf{y}; \mathbf{u}_{\mathbf{Y}}, \mathbf{V}_{\mathbf{Y}})$ with $\mathbf{V}_{\mathbf{Y}} \succ 0$, the inferred message of \mathbf{X} following the sum-product rule is given by

$$\begin{aligned}
\mu_{\mathbf{X}}(\mathbf{x}) &= \int \delta(\mathbf{y} - \mathbf{A} \mathbf{x}) \mu_{\mathbf{Y}}(\mathbf{y}) d\mathbf{y} = f_{\mathbf{Y}}^{\mathbf{E}}(\mathbf{A} \mathbf{x}; \mathbf{u}_{\mathbf{Y}}, \mathbf{V}_{\mathbf{Y}}), \\
&= s_{\mathbf{Y}}^{\mathbf{X}} \cdot f_{\mathbf{X}}^{\mathbf{E}}(\mathbf{x}; \mathbf{u}_{\mathbf{X}}, \mathbf{V}_{\mathbf{X}}), \quad (17a)
\end{aligned}$$

where

$$\mathbf{u}_{\mathbf{X}} = \mathbf{A}^T \mathbf{u}_{\mathbf{Y}}, \quad \mathbf{V}_{\mathbf{X}} = \mathbf{A}^T \mathbf{V}_{\mathbf{Y}} \mathbf{A}, \quad (17b)$$

and the scaling factor $s_{\mathbf{Y}}^{\mathbf{X}}$ is given by

$$s_{\mathbf{Y}}^{\mathbf{X}} = (|\mathbf{V}_{\mathbf{Y}}| / |\mathbf{V}_{\mathbf{X}}|_+)^{1/2}. \quad (17c)$$

Proof. See Appendix B-B. \square

For $m = n$, $\mathbf{V}_{\mathbf{Y}} \succ 0$ ensures $\mathbf{V}_{\mathbf{X}} \succ 0$ (since \mathbf{A} is full-rank), making the inverse mapping of $\mathbf{Y} = \mathbf{A} \mathbf{X}$ unique and straightforward to compute. In this case, (17a)-(17c) can be directly obtained following [30, Eq. (356), (357)].

Lemma 3 (Product of multiple Gaussian densities). The product of K Gaussian PDFs for \mathbf{X} : $f_{\mathbf{X}}^{\mathbf{E}}(\mathbf{x}; \mathbf{u}_{\mathbf{X}_i}, \mathbf{V}_{\mathbf{X}_i})$, where $\text{rank}(\mathbf{V}_{\mathbf{X}_i}) = k_i$, for $i = 1, \dots, K$, is given by

$$\prod_{i=1}^K f_{\mathbf{X}}^{\mathbf{E}}(\mathbf{x}; \mathbf{u}_{\mathbf{X}_i}, \mathbf{V}_{\mathbf{X}_i}) = s_{\mathbf{X}_{1:K}} \cdot f_{\mathbf{X}}^{\mathbf{E}}(\mathbf{x}; \mathbf{u}_{\mathbf{X}}, \mathbf{V}_{\mathbf{X}}) \quad (18a)$$

⁵This full-rank assumption does not lose generality. If \mathbf{A} is rank-deficient, i.e., $k = \text{rank}(\mathbf{A}) < \min(n, m)$, a (rank) decomposition $\mathbf{A} = \mathbf{B} \mathbf{C}$ can be obtained (e.g., using compact singular value decomposition (SVD)) where $\mathbf{B} \in \mathbb{R}^{m \times k}$ and $\mathbf{C} \in \mathbb{R}^{k \times n}$ have full rank ($= k$). Thus, $\mathbf{Y} = \mathbf{A} \mathbf{X} = \mathbf{B}(\mathbf{C} \mathbf{X})$ can be treated as two consecutive linear mapping via full-rank matrices.

where

$$\mathbf{u}_{\mathbf{X}} = \sum_{i=1}^K \mathbf{u}_{\mathbf{X}_i}, \quad \mathbf{V}_{\mathbf{X}} = \sum_{i=1}^K \mathbf{V}_{\mathbf{X}_i}, \quad (18b)$$

and the scaling factor $s_{\mathbf{X}_{1:K}}$ is, with $k = \text{rank}(\mathbf{V}_{\mathbf{X}})$,

$$s_{\mathbf{X}_{1:K}} = \frac{\prod_{i=1}^K |\mathbf{V}_{\mathbf{X}_i}|_+^{1/2}}{(2\pi)^{(\sum_{i=1}^K k_i - k)/2} |\mathbf{V}_{\mathbf{X}}|_+^{1/2}} \exp\left(-\alpha_{\mathbf{X}} + \sum_{i=1}^K \alpha_{\mathbf{X}_i}\right). \quad (18c)$$

Proof. See Appendix B-C. \square

Remark 3. The objective of Problem 1 can be achieved by applying Lemma 2 and Lemma 3, with the scaling factor computations (17c) and (18c) replaced respectively by

$$s_{\mathbf{Y}}^{\mathbf{X}} = |\mathbf{V}_{\mathbf{Y}}|_+^{1/2} \quad (19)$$

and

$$s_{\mathbf{X}_{1:K}} = \frac{\exp(-\alpha_{\mathbf{X}} + \sum_{i=1}^K \alpha_{\mathbf{X}_i})}{(2\pi)^{(\sum_{i=1}^K k_i - k)/2} |\mathbf{V}_{\mathbf{X}}|_+^{1/2}}. \quad (20)$$

These replacements avoid the computation of $|\mathbf{V}_{\mathbf{X}_i}|_+$ while preserving the results.

C. Message Passing Algorithm

With the key computation rules in place, the message passing steps ①–⑤ are detailed below, followed by a brief description of the optional steps ⑥–⑨. Note that steps ⑧ and ⑨ are identical to steps ⑤ and ⑥ in [1, Section IV.A], and detailed computations can be found there. A Gaussian random variable is treated as a special case ($n = 1$) of a Gaussian random vector, reusing the notations.

Step ①: The message $p_{\Lambda_i}(\lambda_i)$ is sent from the leaf node to the variable node Λ_i and then directly to F_i .

Step ②: Factor node F_i sends the following message, 1D GM consisting of two terms, to variable node B_i :

$$\begin{aligned} \mu_{F_i \rightarrow B_i}(b_i) &= \sum_{\lambda_i=0,1} p_{B_i|\Lambda_i=\lambda_i}(b_i) p_{\Lambda_i}(\lambda_i) \\ &= (1 - \theta_i) f_{B_i}(b_i; 0, 0) + \theta_i f_{B_i}(b_i; m_{b,i}, \sigma_{b,i}^2). \end{aligned} \quad (21)$$

This prior PDF of B_i is passed directly to factor node G_i .

Step ③: Factor node G_i sends the following message to variable node Γ_i :

$$\mu_{G_i \rightarrow \Gamma_i}(\gamma_i) = \int G_i \cdot \mu_{F_i \rightarrow B_i}(b_i) db_i,$$

where $G_i = p_{Y_i|\Gamma_i=\gamma_i, B_i=b_i}(y_i) = f_{Y_i}(y_i; \gamma_i + b_i, \sigma_{n,i}^2) = f_{B_i}(b_i; y_i - \gamma_i, \sigma_{n,i}^2)$. Following [1, Eqs. (15)-(16)], the integration results in a 1D GM density with two terms for Γ_i :

$$\begin{aligned} \mu_{G_i \rightarrow \Gamma_i}(\gamma_i) &= (1 - \theta_i) f_{\Gamma_i}(\gamma_i; y_i, \sigma_{n,i}^2) \\ &\quad + \theta_i f_{\Gamma_i}(\gamma_i; y_i - m_{b,i}, \sigma_{n,i}^2 + \sigma_{b,i}^2). \end{aligned} \quad (22)$$

This message is passed directly to factor node K_i .

Step ④: Factor node K_i sends the following message to variable node \mathbf{X} :

$$\mu_{K_i \rightarrow \mathbf{X}}(\mathbf{x}) = \int \delta(\gamma_i - \mathbf{h}_i^T \mathbf{x}) \cdot \mu_{G_i \rightarrow \Gamma_i}(\gamma_i) d\gamma_i.$$

Applying the computations rules (17a), (17b), and (19),

$$\mu_{K_i \rightarrow \mathbf{X}}(\mathbf{x}) \propto \sum_{l=1,2} w_{\mathbf{X}_i}^{(l)} f_{\mathbf{X}}^E(\mathbf{x}; \mathbf{u}_{\mathbf{X}_i}^{(l)}, \mathbf{V}_{\mathbf{X}_i}^{(l)}) \quad (23)$$

where

$$w_{\mathbf{X}_i}^{(1)} = \frac{1 - \theta_i}{\sigma_{n,i}}, \quad w_{\mathbf{X}_i}^{(2)} = \frac{\theta_i}{(\sigma_{n,i}^2 + \sigma_{b,i}^2)^{1/2}}, \quad (24a)$$

$$\mathbf{u}_{\mathbf{X}_i}^{(1)} = \frac{y_i}{\sigma_{n,i}} \mathbf{h}_i, \quad \mathbf{u}_{\mathbf{X}_i}^{(2)} = \frac{y_i - m_{b,i}}{\sigma_{n,i}^2 + \sigma_{b,i}^2} \mathbf{h}_i \quad (24b)$$

$$\mathbf{V}_{\mathbf{X}_i}^{(1)} = \frac{1}{\sigma_{n,i}^2} \mathbf{h}_i \mathbf{h}_i^T, \quad \mathbf{V}_{\mathbf{X}_i}^{(2)} = \frac{1}{\sigma_{n,i}^2 + \sigma_{b,i}^2} \mathbf{h}_i \mathbf{h}_i^T, \quad (24c)$$

Since the α parameter of \mathbf{X}_i is the same as that of K_i , we have

$$\alpha_{\mathbf{X}_i}^{(1)} = -\frac{1}{2} \frac{y_i^2}{\sigma_{n,i}^2}, \quad \alpha_{\mathbf{X}_i}^{(2)} = -\frac{1}{2} \frac{(y_i - m_{b,i})^2}{\sigma_{n,i}^2 + \sigma_{b,i}^2} \quad (25)$$

The GM model (23) for $\mathbf{X} \in \mathbb{R}^4$ consists of two degenerate Gaussian densities in a 1D subspace.

Step ⑤: Node \mathbf{X} computes the product of all the messages sent to it: $\mu_{\mathbf{X}}(\mathbf{x}) \propto \prod_{j=1}^M \mu_{K_j \rightarrow \mathbf{X}}(\mathbf{x})$. Since each message is a GM of two terms, the result is a GM of $L \triangleq 2^M$ terms:

$$\begin{aligned} \mu_{\mathbf{X}}(\mathbf{x}) &\propto \prod_{j=1}^M \left(\sum_{l_j=1,2} w_{\mathbf{X}_j}^{(l_j)} f_{\mathbf{X}}^E(\mathbf{x}; \mathbf{u}_{\mathbf{X}_j}^{(l_j)}, \mathbf{V}_{\mathbf{X}_j}^{(l_j)}) \right) \\ &\propto \sum_{l=1}^L w_{\mathbf{X}}^{(l)} f_{\mathbf{X}}^E(\mathbf{x}; \mathbf{u}_{\mathbf{X}}^{(l)}, \mathbf{V}_{\mathbf{X}}^{(l)}). \end{aligned} \quad (26)$$

Each term of (26) is computed as following: For $l_j \in \{1, 2\}$, $j = 1, \dots, M$, $l \leftarrow 1 + \sum_{j=1}^M (l_j - 1) 2^{j-1}$, and

$$w_{\mathbf{X}}^{(l)} f_{\mathbf{X}}^E(\mathbf{x}; \mathbf{u}_{\mathbf{X}}^{(l)}, \mathbf{V}_{\mathbf{X}}^{(l)}) \propto \prod_{j=1}^M w_{\mathbf{X}_j}^{(l_j)} f_{\mathbf{X}_j}^E(\mathbf{x}; \mathbf{u}_{\mathbf{X}_j}^{(l_j)}, \mathbf{V}_{\mathbf{X}_j}^{(l_j)}),$$

where, following (18a), (18b), and (20),

$$\mathbf{u}_{\mathbf{X}}^{(l)} = \sum_{j=1}^M \mathbf{u}_{\mathbf{X}_j}^{(l_j)}, \quad \mathbf{V}_{\mathbf{X}}^{(l)} = \sum_{j=1}^M \mathbf{V}_{\mathbf{X}_j}^{(l_j)}, \quad (27a)$$

and

$$w_{\mathbf{X}}^{(l)} = s_{\mathbf{X}}^{(l)} \prod_{j=1}^M w_{\mathbf{X}_j}^{(l_j)}, \quad (27b)$$

where, after omitting the constant $(2\pi)^{(\sum_{i=1}^K k_i - k)/2}$ in (20), the scaling factor is given by

$$s_{\mathbf{X}}^{(l)} = \frac{1}{|\mathbf{V}_{\mathbf{X}}^{(l)}|_+^{1/2}} \exp\left(-\alpha_{\mathbf{X}}^{(l)} + \sum_{j=0}^M \alpha_{\mathbf{X}_j}^{(l_j)}\right). \quad (27c)$$

Step ⑥: Variable node \mathbf{X} sends a message $\mu_{\mathbf{X} \rightarrow K_i}(\mathbf{x}) \propto \prod_{j \neq i} \mu_{K_j \rightarrow \mathbf{X}}(\mathbf{x})$ to factor node K_i . The computation follows the same rules as step ⑤ and result in a GM of 2^{M-1} terms.

Step ⑦: Factor node K_i converts $\mu_{\mathbf{X} \rightarrow K_i}(\mathbf{x})$ to $\mu_{K_i \rightarrow \Gamma_i}(\gamma_i)$, a 1D GM model of Γ_i . Each term of $\mu_{\mathbf{X} \rightarrow K_i}(\mathbf{x})$ is converted to a Gaussian density of Γ_i following the linear mapping⁶ $\Gamma_i = \mathbf{h}_i^T \mathbf{X}$, while retaining its weight. This message is sent to Γ_i and then directly to factor node G_i .

Step ⑧: Factor node G_i sends $\mu_{G_i \rightarrow B_i}(b_i)$, a 1D GM model of 2^{M-1} terms, to variable node B_i and then to F_i .

Step ⑨: Factor node F_i sends a message $\mu_{F_i \rightarrow \Lambda_i}(\lambda_i)$, which is the posterior PMF of Λ_i after normalization, to variable node Λ_i . Specifically, the posterior probability of measurement y_i being faulty is given by

$$\theta_i' \triangleq \frac{\mu_{F_i \rightarrow \Lambda_i}(\lambda_i = 1)}{\mu_{F_i \rightarrow \Lambda_i}(\lambda_i = 0) + \mu_{F_i \rightarrow \Lambda_i}(\lambda_i = 1)}. \quad (28)$$

A few notes are in order regarding step ⑤. First, if $M \geq 4$ and the measurement vectors $\mathbf{h}_1, \mathbf{h}_2, \dots, \mathbf{h}_M$ are linearly independent, the matrices $\mathbf{V}_{\mathbf{X}}^{(l)}$, $l = 1, \dots, L$, calculated in (27a), are guaranteed to be positive definite. Consequently, the pseudo-inverse and pseudo-determinant of $\mathbf{V}_{\mathbf{X}}^{(l)}$ simplify to the regular inverse and determinant, making the computation

⁶The Gaussian message passing rule for the linear mapping $\mathbf{Y} = \mathbf{A}\mathbf{X}$ is trivial. Given $\mu_{\mathbf{X}}(\mathbf{x}) = f_{\mathbf{X}}(\mathbf{x}; \mathbf{m}_{\mathbf{X}}, \Sigma_{\mathbf{X}})$, the inferred message for \mathbf{Y} is $\mu_{\mathbf{Y}}(\mathbf{y}) = f_{\mathbf{Y}}(\mathbf{y}; \mathbf{m}_{\mathbf{Y}}, \Sigma_{\mathbf{Y}})$ where $\mathbf{m}_{\mathbf{Y}} = \mathbf{A}\mathbf{m}_{\mathbf{X}}$ and $\Sigma_{\mathbf{Y}} = \mathbf{A}\Sigma_{\mathbf{X}}\mathbf{A}^T$.

of $|\mathbf{V}_{\mathbf{X}}^{(l)}|_+ \equiv |\mathbf{V}_{\mathbf{X}}^{(l)}|$ in (27c) straightforward. Additionally, the covariance matrix $\Sigma_{\mathbf{X}}^{(l)} = (\mathbf{V}_{\mathbf{X}}^{(l)})^+ \equiv (\mathbf{V}_{\mathbf{X}}^{(l)})^{-1}$ and mean vector $\mathbf{m}_{\mathbf{X}}^{(l)} = (\mathbf{V}_{\mathbf{X}}^{(l)})^{-1} \mathbf{u}$ can also be easily computed for all l . Thus, we can rewrite (26) using Gaussian PDFs $f_{\mathbf{X}}(\mathbf{x}; \mathbf{m}_{\mathbf{X}}^{(l)}, \Sigma_{\mathbf{X}}^{(l)})$ instead. Second, if a prior PDF $p_{\mathbf{X}}(\mathbf{x})$ is available, it should be multiplied to $\mu_{\mathbf{X}}(\mathbf{x})$. This computation can be easily performed if $p_{\mathbf{X}}(\mathbf{x})$ is a Gaussian distribution or GM. Third, the weights $\{w_{\mathbf{X}}^{(l)}\}$ given by (27b) do not necessarily sum to one, so a normalization step is required. We reuse $w_{\mathbf{X}}^{(l)}$ for the normalized weight to avoid introducing extra symbols. The exact PDF of \mathbf{X} can be obtained from $\mu_{\mathbf{X}}(\mathbf{x})$ as follows:

$$p_{\mathbf{X}}^{\text{pos}}(\mathbf{x}) = \sum_{l=1}^L w_{\mathbf{X}}^{(l)} f_{\mathbf{X}}(\mathbf{x}; \mathbf{m}_{\mathbf{X}}^{(l)}, \Sigma_{\mathbf{X}}^{(l)}). \quad (29)$$

Remark 4 (Complexity). The computational complexity of the message passing process scales with M . The primary computational cost for the mandatory steps arises from step ④, which is performed in parallel for each measurement, and step ⑤, which is performed only once. Among the optional steps, step ⑥ is the most computationally intensive, followed by step ⑦. Fortunately, most operations in these steps involve simple vector/matrix addition and multiplication, and many of the results can be reused in steps ⑤ and ⑥.

D. No Measurement Exclusion

In [1], we proposed excluding a measurement y_i if its posterior fault probability exceeds a threshold θ_T and using the posterior PDF of \mathbf{X} computed with the remaining measurements, i.e., $p_{\mathbf{X}}^{\text{ex}}(\mathbf{x}) \propto \prod_{j \in \mathcal{I}_{\text{ex}}^c} \mu_{K_j \rightarrow \mathbf{X}}(\mathbf{x})$, where $\mathcal{I}_{\text{ex}}^c \triangleq \{1 \leq i \leq M : \theta_i' \leq \theta_T\}$, instead of (29) for PL computation. However, this approach can compromise integrity requirements. Indeed, measurement exclusion is unnecessary since all information about the UE position and measurement states is captured in $p_{\mathbf{X}}^{\text{pos}}(\mathbf{x}) \propto \prod_{j=1}^M \mu_{K_j \rightarrow \mathbf{X}}(\mathbf{x})$. In fact, if exclusion is performed, the conditional pointwise mutual information (C-PMI) between \mathbf{X} and the excluded measurements, given the remaining measurements, must be considered to maintain integrity requirements. To elaborate, we revisit the nature of the problem: In each positioning epoch, the position $\mathbf{x} \in \mathbb{R}^n$ and the measurement $\mathbf{y} \in \mathbb{R}^M$ are generated according to their joint probability PDF $p_{\mathbf{X}, \mathbf{Y}}(\mathbf{x}, \mathbf{y})$. Based on the posterior PDF $p_{\mathbf{X}|\mathbf{Y}=\mathbf{y}}(\mathbf{x})$, a n -dimensional ball $\mathcal{B}(\mathbf{y})$, centered at $\hat{\mathbf{x}}$ with radius PL, is determined to satisfy the requirement $\int p_{\mathbf{X}|\mathbf{Y}=\mathbf{y}}(\mathbf{x}) I(\mathbf{x} \in \mathcal{B}(\mathbf{y})) d\mathbf{x} \geq 1 - P_{\text{TIR}}$, where $I(\cdot)$ stands for the indicator function. The integrity probability, which is the reciprocal of the integrity risk and can be expressed as

$$\begin{aligned} P_1 &= \int \int p_{\mathbf{X}, \mathbf{Y}}(\mathbf{x}, \mathbf{y}) I(\mathbf{x} \in \mathcal{B}(\mathbf{y})) d\mathbf{x} d\mathbf{y} \\ &= \int p_{\mathbf{Y}}(\mathbf{y}) \left(\int p_{\mathbf{X}|\mathbf{Y}=\mathbf{y}}(\mathbf{x}) I(\mathbf{x} \in \mathcal{B}(\mathbf{y})) d\mathbf{x} \right) d\mathbf{y} \end{aligned}$$

is ensured to be $\geq 1 - P_{\text{TIR}}$.

As an example, let us consider that for a set of measurements, we have a rule to exclude the first measurement y_1 . Then, in the realizations where the rule establishes that measurement y_1 has to be removed, a n -dimensional ball $\tilde{\mathcal{B}}(\bar{\mathbf{y}})$ is obtained based on the the posterior PDF $p_{\mathbf{X}|\bar{\mathbf{Y}}=\bar{\mathbf{y}}}(\mathbf{x})$, where $\bar{\mathbf{y}} \triangleq [y_2, \dots, y_M]^T$. This exclusion rule corresponds to region $\mathcal{D} \in \mathbb{R}^M$: If $\mathbf{y} \in \mathcal{D}$, y_1 is excluded. Letting $\mathcal{D}^c \triangleq \mathbb{R}^M \setminus \mathcal{D}$, the

integrity probability decomposes as $P_1 = P_{1,1} + P_{1,2}$ where $P_{1,1} = \int_{\mathbf{y} \in \mathcal{D}^c} p_{\mathbf{Y}}(\mathbf{y}) \left(\int p_{\mathbf{X}|\mathbf{Y}=\mathbf{y}}(\mathbf{x}) I(\mathbf{x} \in \mathcal{B}(\mathbf{y})) d\mathbf{x} \right) d\mathbf{y}$ and $P_{1,2} = \int_{\mathbf{y} \in \mathcal{D}} p_{\mathbf{Y}}(\mathbf{y}) \left(\int p_{\mathbf{X}|\mathbf{Y}=\mathbf{y}}(\mathbf{x}) I(\mathbf{x} \in \tilde{\mathcal{B}}(\bar{\mathbf{y}})) d\mathbf{x} \right) d\mathbf{y}$. Since

$$\begin{aligned} &\int p_{\mathbf{X}|\mathbf{Y}=\mathbf{y}}(\mathbf{x}) I(\mathbf{x} \in \tilde{\mathcal{B}}(\bar{\mathbf{y}})) d\mathbf{x} \\ &= \int \underbrace{\frac{p_{\mathbf{X}, Y_1|\bar{\mathbf{Y}}=\bar{\mathbf{y}}}(\mathbf{x}, y_1)}{p_{\mathbf{X}|\bar{\mathbf{Y}}=\bar{\mathbf{y}}}(\mathbf{x}) p_{Y_1|\bar{\mathbf{Y}}=\bar{\mathbf{y}}}(y_1)}}_{\text{C-PMI}} p_{\mathbf{X}|\bar{\mathbf{Y}}=\bar{\mathbf{y}}}(\mathbf{x}) I(\mathbf{x} \in \tilde{\mathcal{B}}(\bar{\mathbf{y}})) d\mathbf{x}, \end{aligned}$$

and the C-PMI term, which measures the dependence between \mathbf{X} and Y_1 given $\bar{\mathbf{Y}} = \bar{\mathbf{y}}$, can be either greater or less than 1, $P_{1,1} + P_{1,2} \geq 1 - P_{\text{TIR}}$ is *generally not guaranteed*⁷ given that $\tilde{\mathcal{B}}(\bar{\mathbf{y}})$ meets the requirement $\int p_{\mathbf{X}|\bar{\mathbf{Y}}=\bar{\mathbf{y}}}(\mathbf{x}) I(\mathbf{x} \in \tilde{\mathcal{B}}(\bar{\mathbf{y}})) d\mathbf{x} \geq 1 - P_{\text{TIR}}$. Intuitively, the issue is that we use the information in y_1, \dots, y_M to exclude y_1 but then use $p_{\mathbf{X}|\bar{\mathbf{Y}}=\bar{\mathbf{y}}}(\mathbf{x})$ for PL computation as if y_1 never existed, but $p_{\mathbf{X}|\bar{\mathbf{Y}}=\bar{\mathbf{y}}}(\mathbf{x})$ is not the actual posterior PDF of \mathbf{X} because y_1 existed and the whole vector \mathbf{y} was such that it triggered the exclusion rule.

V. BAYESIAN RAIM PART II: PL COMPUTATION

The exact posterior PDF given by (29) allows for position estimation and PLs computation for 3D or any lower-dimensional subspace as defined in Definition 1. Exact 1D PLs and 2D/3D overestimates can be obtained using methods similar to those described in Section III-D. However, calculating exact 2D/3D PLs is more challenging. In this section presents methods for both tasks.

A. Exact 1D PL and 2D/3D PL Overestimates

Since this work does not focus on position estimation methods, the Bayesian RAIM algorithm simply computes the weighted mean, $\bar{\mathbf{m}}_{\mathbf{X}} \triangleq \sum_{l=1}^L w_{\mathbf{X}}^{(l)} \mathbf{m}_{\mathbf{X}}^{(l)}$, as the estimate of \mathbf{x} . Thus, the 3D position estimate is given by $\hat{\mathbf{x}}_{\mathbf{u}} = [\bar{\mathbf{m}}_{\mathbf{X}}]_{1:3} = \sum_{l=1}^L w_{\mathbf{X}}^{(l)} [\mathbf{m}_{\mathbf{X}}^{(l)}]_{1:3}$. Based on (29), we can immediately obtain the PDFs of the positioning error vectors \mathbf{e}_{nD} for any $\mathcal{L}(\tilde{\mathbf{v}}_1)$ ($n = 1$), $\mathcal{P}(\tilde{\mathbf{v}}_1, \tilde{\mathbf{v}}_2)$ ($n = 2$), or \mathbb{R}^3 ($n = 3$), which are all GMs with the same number of terms and weights as (29). Specifically, for the 3D positioning error vector \mathbf{e}_{3D} :

$$p_{\mathbf{E}_{3D}}(\mathbf{e}_{3D}) = \sum_{l=1}^L w_{\mathbf{X}}^{(l)} f_{\mathbf{E}_{3D}}(\mathbf{e}_{3D}; \mathbf{m}_{3D}^{(l)}, \Sigma_{3D}^{(l)}), \quad (30)$$

where, for $l = 1, \dots, L$,

$$\mathbf{m}_{3D}^{(l)} = [\mathbf{m}_{\mathbf{X}}^{(l)}]_{1:3} - \hat{\mathbf{x}}_{\mathbf{u}}, \quad \Sigma_{3D}^{(l)} = [\Sigma_{\mathbf{X}}^{(l)}]_{1:3, 1:3}. \quad (31)$$

Letting $\tilde{\mathbf{v}}_{1D} = [\tilde{\mathbf{v}}_1]$ and $\tilde{\mathbf{v}}_{2D} = [\tilde{\mathbf{v}}_1 \ \tilde{\mathbf{v}}_2]$, the PDFs of \mathbf{e}_{1D} and \mathbf{e}_{2D} are given by

$$p_{\mathbf{E}_{nD}}(\mathbf{e}_{nD}) = \sum_{l=1}^L w_{\mathbf{X}}^{(l)} f_{\mathbf{E}_{nD}}(\mathbf{e}_{nD}; \mathbf{m}_{nD}^{(l)}, \Sigma_{nD}^{(l)}), \quad (32)$$

where $n = 1, 2$, and for $l = 1, \dots, L$,

$$\mathbf{m}_{nD}^{(l)} = \tilde{\mathbf{v}}_{nD}^T \mathbf{m}_{3D}^{(l)}, \quad \Sigma_{nD}^{(l)} = \tilde{\mathbf{v}}_{nD}^T \Sigma_{3D}^{(l)} \tilde{\mathbf{v}}_{nD}. \quad (33)$$

To determine the exact 1D PL for the subspace $\mathcal{L}(\tilde{\mathbf{v}}_1)$, we use (32). Given that \mathbf{e}_{1D} , $\mathbf{m}_{1D}^{(l)}$, and $\Sigma_{1D}^{(l)}$ are scalars, we denote them as e_{1D} , $m_{1D}^{(l)}$, and $[\sigma_{1D}^{(l)}]^2$, respectively. Using the Q function, the actual IR associated with $\hat{\mathbf{x}}_{\mathbf{u}}$ and any r in $\mathcal{L}(\tilde{\mathbf{v}}_1)$ is expressed as:

$$\Pr \{|e_{1D}| > r\} = \Pr \{e_{1D} < -r\} + \Pr \{e_{1D} > r\}$$

⁷Actually, it was observed also experimentally that the inequality is violated when an exclusion rule is implemented.

$$= \sum_{l=1}^L w_{\mathbf{X}}^{(l)} \left[1 - Q \left(\frac{-r - m_{1D}^{(l)}}{\sigma_{1D}^{(l)}} \right) + Q \left(\frac{r - m_{1D}^{(l)}}{\sigma_{1D}^{(l)}} \right) \right] \quad (34)$$

The smallest r ensuring $\Pr \{|e_{1D}| > r\} < P_{\text{TIR}}$ is found using bisection search, yielding PL_{1D} . This value represents the most stringent 1D PL for the position estimate $\hat{\mathbf{x}}_u$.

To obtain overestimates for the 2D PL for $\mathcal{P}(\tilde{\mathbf{v}}_1, \tilde{\mathbf{v}}_2)$ and the 3D PL for \mathbb{R}^3 using Lemma 1, we select $w_i = 1/n$ for $i = 1, \dots, n$, and find the smallest r_i that ensures

$$\sum_{l=1}^L w_{\mathbf{X}}^{(l)} \left[1 - Q \left(\frac{-r_i - [\mathbf{m}_{nD}^{(l)}]_i}{[\Sigma_{nD}^{(l)}]_{i,i}^{1/2}} \right) + Q \left(\frac{r_i - [\mathbf{m}_{nD}^{(l)}]_i}{[\Sigma_{nD}^{(l)}]_{i,i}^{1/2}} \right) \right]$$

$$< w_i P_{\text{TIR}}$$

using bisection search and assigned to PL_i . Finally, the overestimate PL_{nD}^U is computed following (6).

B. Exact 2D/3D PL Computation

As discussed in Section II-B, computing the exact 2D/3D PL equivalent to finding the minimum radius of a 2D circle or 3D sphere centered at the origin that includes the positioning error vector \mathbf{e}_{nD} with a probability of at least $1 - P_{\text{TIR}}$. This is a complex problem. In Appendix C, we derive Theorem 1, which provides a formulation for the minimum radius and forms the basis for our PL searching algorithm.

Theorem 1. Given that the n -dimensional positioning error vector \mathbf{e}_{nD} follows a GM distribution with the PDF (30) for $n = 3$ and (32) for $n = 2$, the PL computation problem defined by (4) can be reformulated as:

$$\text{PL}_{nD} = \min \left\{ r \left| \sum_{l=1}^L w_{\mathbf{X}}^{(l)} [1 - F_{Z_l}(r^2)] < P_{\text{TIR}} \right. \right\}, \quad (35)$$

where $F_{Z_l}(z) \triangleq \Pr \{Z_l \leq z\}$, $l = 1, \dots, L$, represents the cumulative density function (CDF) of a random variable Z_l , given by a weighted sum of n independent noncentral chi-square distributed random variables $W_{l,1}, \dots, W_{l,n}$, each with one degree of freedom and noncentrality parameter $\nu_{l,i}^2$. Specifically,

$$Z_l = \sum_{i=1}^n \omega_{l,i} W_{l,i}, \quad W_{l,i} \sim \chi^2(1, \nu_{l,i}^2), \quad \forall i = 1, \dots, n; \quad (36)$$

and $\{\omega_{l,i}\}$ and $\{\nu_{l,i}^2\}$ are determined by $\Sigma_{nD}^{(l)}$ and $\mathbf{m}_{nD}^{(l)}$ in the following way: Perform eigendecomposition to obtain $\Sigma_{nD}^{(l)} = \mathbf{P}_l \Omega_l \mathbf{P}_l^T$, where $\mathbf{P}_l \in \mathbb{R}^{n \times n}$ is an orthogonal matrix and Ω_l is a diagonal matrix. The diagonal elements of Ω_l are $\omega_{l,1}, \dots, \omega_{l,n}$ (since $\Sigma_{nD}^{(l)} > 0$, $\omega_{l,i} > 0$ for $i = 1, \dots, n$); and the noncentrality parameters $\nu_{l,1}, \dots, \nu_{l,n}$ are computed by $(\nu_{l,1}, \dots, \nu_{l,n})^T \triangleq \mathbf{P}_l^T [\Sigma_{nD}^{(l)}]^{-\frac{1}{2}} \mathbf{m}_{nD}^{(l)}$.

Proof. See Appendix C. \square

There is no closed-form expression for the CDF of a generalized chi-squared variable, but numerical methods are available. In Appendix D, we describe the Imhof method [31], a numerical method that can achieve arbitrary accuracy. The CDF $F_{Z_l}(z)$ can be approximated by:

$$\bar{F}_{Z_l}(z, U_l) = \frac{1}{2} - \frac{1}{\pi} \int_0^{U_l} \frac{\sin \beta(u, z)}{u \kappa(u)} du, \quad (37)$$

where $\beta(u, z)$ and $\kappa(u)$ are given by (51a) and (51b). The approximation error is bounded by

$$|F_{Z_l}(z) - \bar{F}_{Z_l}(z, U_l)| \leq \Xi(U_l) \quad (38)$$

where $\Xi(\cdot)$ is a decreasing function provided in (52). For any desired accuracy, a sufficiently large U_l can be found to ensure $\Xi(U_l)$ meets the requirements. For PL computation, the smallest U_l satisfying $\Xi(U_l) \leq \zeta_1 P_{\text{TIR}}$, where $\zeta_1 \ll 1$, is chosen. To incorporate the approximation error, the constraint in (35) is modified to:

$$\sum_{l=1}^L w_{\mathbf{X}}^{(l)} [1 - \bar{F}_{Z_l}(r^2, U_l)] < (1 - \zeta_1) P_{\text{TIR}}. \quad (39)$$

With this numerical tool, PL_{nD} in (35) can be obtained using a search process similar to the bisection search in Section III-D. In particular, the overestimate PL_{nD}^U serves as a good initial value for R_{up} . Choosing an initial value for R_{low} is trivial. During each iteration, the numerical integral (37) needs to be computed L times, where $L = 2^M$. This can be computationally expensive. To reduce the computational complexity, we sort $\{w_{\mathbf{X}}^{(l)}\}$ in non-increasing order, denoted by $\{w_{\mathbf{X}}^{(l(1))}, w_{\mathbf{X}}^{(l(2))}, \dots, w_{\mathbf{X}}^{(l(L))}\}$. Then we find the smallest integer J such that

$$\sum_{j=J+1}^L w_{\mathbf{X}}^{(l(j))} \leq \zeta_2 P_{\text{TIR}}, \quad (40)$$

where $\zeta_2 \ll 1$. Since $\sum_{l=1}^L w_{\mathbf{X}}^{(l)} [1 - F_{Z_l}(r^2)] < \sum_{j=1}^J w_{\mathbf{X}}^{(l(j))} [1 - F_{Z_{l(j)}}(r^2)] + \sum_{j=J+1}^L w_{\mathbf{X}}^{(l(j))}$, we can replace the constraint in (35) with a stronger one:

$$\sum_{j=1}^J w_{\mathbf{X}}^{(l(j))} [1 - F_{Z_{l(j)}}(r^2)] < (1 - \zeta_2) P_{\text{TIR}}. \quad (41)$$

When using (37) for approximation and choosing U_l as described, (39) becomes

$$\sum_{j=1}^J w_{\mathbf{X}}^{(l(j))} [1 - \bar{F}_{Z_{l(j)}}(r^2, U_{l(j)})] < (1 - \zeta_1 - \zeta_2) P_{\text{TIR}}.$$

The PL search algorithm developed based on the above discussions is summarized in Algorithm 1. Due to conservative approximations, the output is expected to be slightly looser than the optimal PL.

Remark 5 (Complexity). Computing the exact 1D PL via bisection search is computationally efficient, as is the 2D/3D overestimation process. Assuming $N_{\text{it}} > 0$ iterations for a 1D search, the complexity is $\mathcal{O}(2N_{\text{it}}L)$. This complexity can be further reduced by discarding GM terms with negligible weights outlined in (40). However, finding the exact 2D/3D PL using Algorithm 1 has higher complexity due to numerical integration in (37). To ensure accuracy, the upper integration limit U_l is often set to a large value. Additionally, as numerical studies will show, the process is sensitive to the parameters of the general chi-squared variables defined by (36), which are influenced by the measurement bias distributions.

VI. NUMERICAL STUDY

We conduct numerical studies with two objectives: (i), to compare the performance of the proposed Bayesian RAIM algorithm with the baseline RAIM algorithm, and (ii), to assess the sensitivity to initial the positioning error \mathbf{e}_0 .

A. Simulation Setup

1) *Scenario and parameters:* The studies involve $M = 12$ BSs deployed in an approximately 1000×1000 m² area,

Algorithm 1 Exact n -dimensional PL computation, $n = 2, 3$

Input: $P_{\text{TIR}}, p_{E_{nD}}(\mathbf{e}_{nD})$ given by (30) or (32), ζ_1, ζ_2 , search error tolerance r_{tol} .

Output: PL_{nD} defined in (35) within error tolerance r_{tol} .

- 1: Compute the overestimate PL_{nD}^U following Section V-A;
 - 2: Sort $\{w_{\mathbf{x}}^{(l)}\}$ into non-increasing order and find the smallest J satisfying (40);
 - 3: **for** $j = 1, \dots, J$ **do** ▷ Parameter preparation
 - 4: Compute $\{\omega_{l(j),i}\}$ and $\{\nu_{l(j),i}^2\}$ following Theorem 1;
 - 5: Find $U_{l(j)}$ such that $\Xi(U_{l(j)}) = \zeta_1 P_{\text{TIR}}$ based on (52);
 - 6: **end for**
 - 7: $r_{\text{up}} \leftarrow \text{PL}_{nD}^U$; ▷ Starting upper limit for PL_{nD}
 - 8: $r_{\text{low}} \leftarrow$ some small value; ▷ Starting lower limit
 - 9: **while** $|r_{\text{up}} - r_{\text{low}}| > r_{\text{tol}}$ **do**
 - 10: $r_{\text{mid}} \leftarrow (r_{\text{up}} + r_{\text{low}})/2$;
 - 11: $P_{\text{mid}} \leftarrow \sum_{j=1}^J w_{\mathbf{x}}^{(l(j))} [1 - \bar{F}_{Z_{l(j)}}(r_{\text{mid}}^2, U_{l(j)})]$ using (37);
 - 12: **if** $P_{\text{mid}} < (1 - \zeta_1 - \zeta_2)P_{\text{TIR}}$ **then**
 - 13: $r_{\text{up}} \leftarrow r_{\text{mid}}, P_{\text{up}} \leftarrow P_{\text{mid}}$;
 - 14: **else**
 - 15: $r_{\text{low}} \leftarrow r_{\text{mid}}, P_{\text{low}} \leftarrow P_{\text{mid}}$;
 - 16: **end if**
 - 17: **end while**
 - 18: $\text{PL}_{nD} \leftarrow r_{\text{up}}$.
-

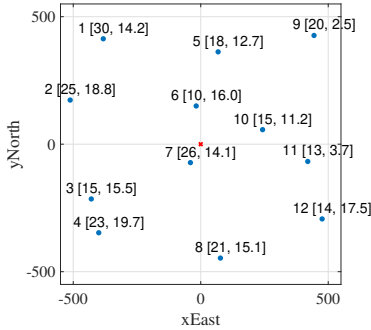


Fig. 3. Simulation scenario layout. BSs are represented using solid blue dots. Their index i , height $x_{i,3}$ (m) and the Gaussian mean of the NLoS-type bias $m_{b,i}$ (m) are provided in the form: $i [x_{i,3}, m_{b,i}]$ above each point.

indicated as solid blue dots in Fig. 3. The BS positions in the x - y plane are given by displacing a 4×3 grid of points, each cell measuring 400×250 meters, with independent Gaussian perturbations $\sim \mathcal{N}(0, 60^2)$ in both x and y directions. The heights ($x_{i,3}$) of the BSs are randomly generated between 10 and 30 m. The true UE position is set at $\mathbf{x}_u = (0, 0, 0)$ with zero clock bias ($x_c = 0$). Measurement noise is identically distributed across all BSs with zero mean, $\sigma_{n,i} = 0.5$ m [7, Annex B2], and a prior fault probability $\theta_i = 0.05$. Two fault types are considered: one due to strong non-line-of-sight (NLoS) signals, with $m_{b,i}$ between 1 and 20 m and $\sigma_{b,i} = 1$ m for all i , and another due to clock synchronization errors with $m_{b,i} = 0$ m and $\sigma_{b,i} = 10$ m for all i . A TIR of $P_{\text{TIR}} = 10^{-3}$ is used for all PL computations. The values of $x_{i,3}$ and $m_{b,i}$ can be found in Fig. 3.

2) *Benchmarks:* For performance comparison, an error-free initial UE position estimate $\mathbf{x}_{u,0} = \mathbf{x}_u$ is used, ensuring no linearization (1) errors. For each fault type, $N_{\text{sim}} = 5 \times 10^5$

positioning epochs are simulated. The Baseline RAIM algorithm computes PLs for the horizontal-plane (H-plane) and the vertical-direction (V-direction) with false alarm probabilities $P_{\text{FA,H}} = P_{\text{FA,V}} = 10^{-2}$. The Bayesian RAIM algorithm computes the horizontal PL overestimate PL_H^U using the method from Section V-A, a near-optimal PL_H using the *exact PL computation* algorithm with $\zeta_1 = 0.1$ and $\zeta_2 = 0.002$, and the optimal PLs for the vertical and the 45° directions in the x - y plane, with unit vector $\tilde{\mathbf{v}}_{45^\circ} = (\cos 45^\circ, \sin 45^\circ, 0)^T$ in the latter case.

For sensitivity study, initial positioning error \mathbf{e}_0 is introduced, such that $\mathbf{x}_{u,0} = \mathbf{x}_u + \mathbf{e}_0$. Two error models are considered: horizontal error $\mathbf{e}_{0,H} = (E_H \cos \phi, E_H \sin \phi, 0)^T$ with ϕ uniformly distributed on $[0, 2\pi)$, and vertical error $\mathbf{e}_{0,V} = (0, 0, E_V)^T$. E_H varies from 0 to 5 m in 0.5 m increments, while E_V varies from -10 to 10 m in 2 m steps. For each value of E_H or E_V , N_{sim} positioning epochs are simulated for each fault type with the same noise and bias realizations. For Bayesian RAIM, we focus only on the vertical direction and on the horizontal $\tilde{\mathbf{v}}_{45^\circ}$ direction.

3) *Performance metrics:* The performance of the algorithms is evaluated using the following metrics:

- 1) *Simulated IR:* Let $\text{PE}_{nD,k} \triangleq \|\mathbf{e}_{nD,k}\|$ and $\text{PL}_{nD,k}$ denote the actual positioning error (PE) and computed PL in the k th epoch, respectively. The simulated IR is defined as:

$$\text{IR}_{nD} = \frac{\sum_{k=1}^{N_{\text{sim}}} I(\text{PE}_{nD,k} > \text{PL}_{nD,k})}{N_{\text{sim}}}, \quad (42)$$

where the indicator function $I(\cdot)$ returns 1 if $\text{PE}_{nD,k} > \text{PL}_{nD,k}$, indicating an integrity failure, and 0 otherwise.

- 2) *PL tightness:* Tighter PL values are preferable. Quantitatively, we evaluated the 50th, 95th, and 99th percentile PL values. For visual comparison, we use the *Stanford diagram* [4]. In this diagram, each epoch contributes a point on the PE-PL plane, with PE_{nD} and PL_{nD} values. Points form a cloud over N_{sim} epochs, ideally located towards the lower-left (indicating lower PE_{nD} and PL_{nD}). Points below the diagonal line in the lower-right half-plane indicate integrity failures. The diagram's resolution and color intensity depend on the pixel density, with each pixel encompasses a small square area.
- 3) *Running time:* Computational complexity is measured by the running time in Matlab on a MacBook Pro with an Intel Core i7 processor. For the Bayesian RAIM algorithm, all nine message passing steps described in Section IV-C are performed.

B. Performance Comparison Study Results

Fig. 4 and Fig. 5 present the simulated results as Stanford diagrams for NLoS- and clock-type faults, respectively. Pixel sizes are detailed in the captions. Both algorithms achieve simulated IRs below the $P_{\text{TIR}} = 10^{-3}$ limit in all subspaces, demonstrating their reliability. Bayesian RAIM consistently provides tighter PLs than Baseline RAIM, despite noticeable variations in the point cloud shapes between subspaces and fault types. The percentile values of the horizontal overestimate PL_H^U and the near-optimal PL_H , along with their reduction relative to Baseline RAIM, are provided in Table I.

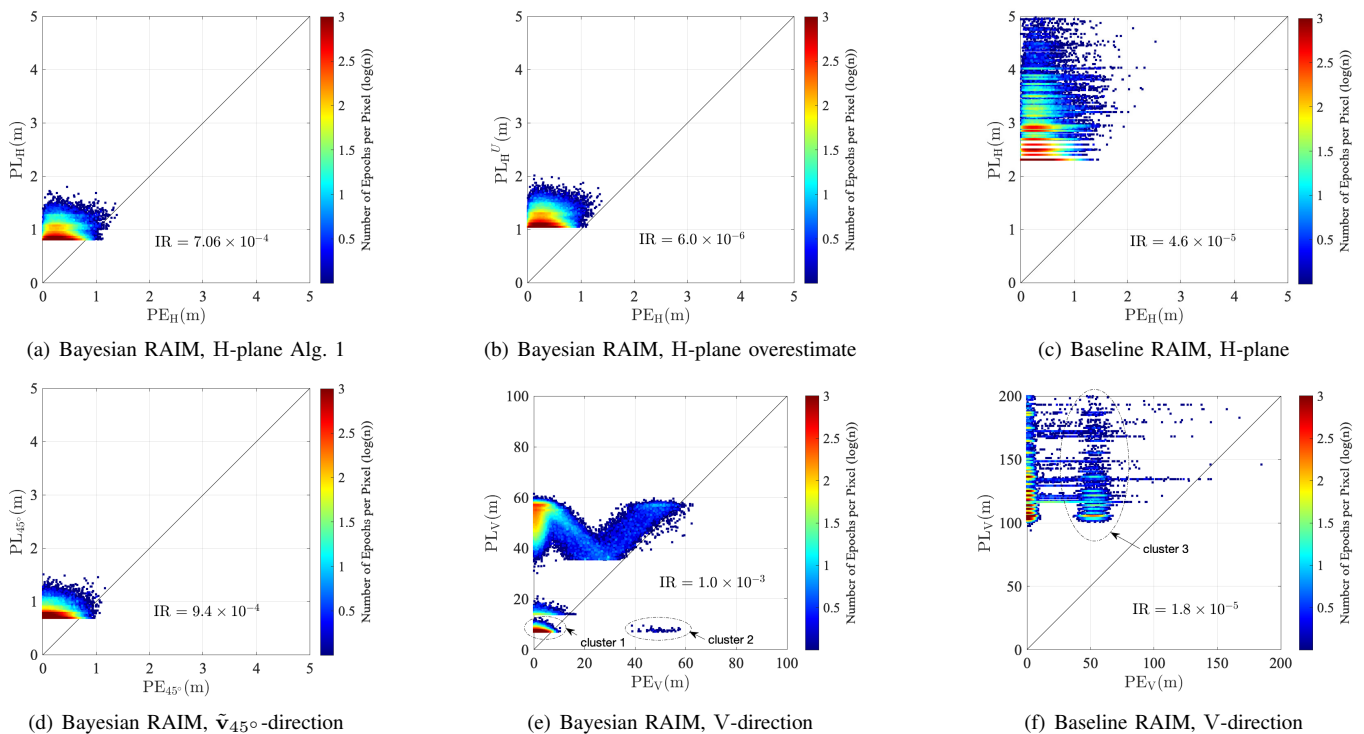


Fig. 4. Performances of the RAIM algorithms in the form of Stanford diagrams under NLoS type fault conditions, with same TIR requirement $P_{\text{TIR}} = 10^{-3}$ for all subspaces. In (a)-(d), a pixel stands for $0.01 \times 0.01 \text{ m}^2$; in (e) and (f), a pixel stands for $0.2 \times 0.2 \text{ m}^2$.

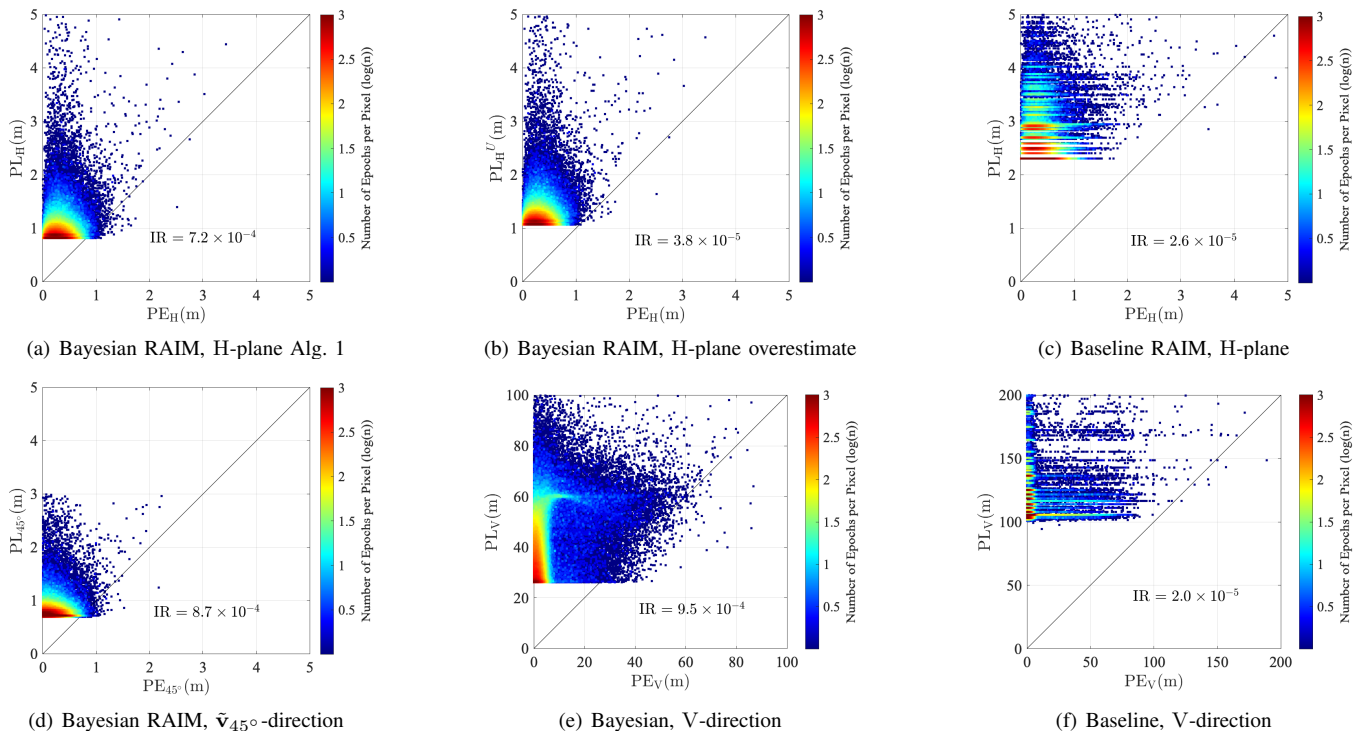


Fig. 5. Performances of the RAIM algorithms in the form of Stanford diagrams under clock synchronization type fault conditions, with same TIR requirement $P_{\text{TIR}} = 10^{-3}$ for all subspaces. In (a)-(d), a pixel stands for $0.01 \times 0.01 \text{ m}^2$; in (e) and (f), a pixel stands for $0.2 \times 0.2 \text{ m}^2$.

1) *H-plane*: The well-distributed BSs around the UE provide strong positioning capability on the H-plane. In Fig. 4 and Fig. 5, subfigures (a)-(c), Baseline RAIM achieves simulated IRs in the order of 10^{-5} for both fault types. Bayesian RAIM achieves similar IRs using PL overestimation and just below P_{TIR} using the exact PL computation algorithm. While fault types minimally affect Baseline RAIM, clock-type faults

causes larger PLs in Bayesian RAIM, spreading the point clouds upwards due to the inseparable small bias realizations from noise. Table I shows that Bayesian RAIM achieved over 50% PL reduction for all percentiles with the overestimation method and over 60% with the exact PL computation method, except for the 99th percentile value under clock-type faults.

TABLE I

EMPIRICAL PERCENTILE PL VALUES (v) AND REDUCTION (r , COMPUTED BY $r = 1 - \text{PL}_{\text{Bayesian}}/\text{PL}_{\text{Baseline}}$) BY BAYESIAN RAIM COMPARED TO BASELINE RAIM: N DENOTES NLOS-TYPE FAULT, AND C DENOTES CLOCK-TYPE FAULT.

		PL@50%		PL@95%		PL@99%	
		v [m]	r [%]	v [m]	r [%]	v [m]	r [%]
PL _H ^U	N	1.10	52.4	1.32	59.1	1.46	62.5
	C	1.14	50.6	1.44	51.8	1.80	51.7
PL _H	N	0.84	63.5	1.07	66.7	1.22	68.7
	C	0.88	61.7	1.18	60.5	1.55	58.4
PL _V	N	7.32	93.1	56.53	58.5	57.48	65.9
	C	34.12	67.7	58.63	56.4	67.81	55.0

2) \tilde{v}_{45° -direction: In both Fig. 4 and Fig. 5, subfigure (d) shows tighter PLs and simulated IRs closer to P_{TIR} compared to subfigure (a), highlighting the advantage of Bayesian RAIM when the direction of interest is known.

3) V -direction: In both figures, subfigures (e) and (f) show Baseline RAIM achieving simulated IRs in the order of 10^{-5} , while Bayesian RAIM remains close to 10^{-3} . The relatively low BS heights reduce vertical positioning capability, resulting in significantly larger PL values compared to the H-plane. Point clouds vary significantly in shape depending on the algorithm and fault type, influenced by BS geometry. Notably, they cluster into distinct groups under NLoS-type fault conditions in Fig. 4(e) and (f), due to the proximity of the 7th BS to the UE, making its large measurement biases influential. Specifically, in Fig. 4(e), cluster 1 is generated by approximately 3.44×10^5 epochs where the 7th measurement is fault-free; and cluster 2 consists of 51 epochs where the 7th measurement is faulty but has a low posterior fault probability θ'_i (28), resulting in too small PLs to upper bound the PEs. In Fig. 4(f), cluster 3 consists mainly of epochs with fault modes where the 7th measurement is incorrectly excluded or faulty but not detected. Despite this, Bayesian RAIM consistently produces much lower PL values compared to Baseline RAIM for both fault types, with reductions ranging from 55.0% to 93.1%, as shown in Table I.

4) *Running time*: The empirical CDF results for total and PL computation times of Baseline RAIM and Bayesian RAIM with PL overestimation are shown in Fig. 6. Fault types have little impact on these results. Baseline RAIM's total running time varies significantly and can exceed that of Bayesian RAIM with overestimation, which has consistent runtimes with a median around 0.55 seconds. PL overestimation contributes minimally to both algorithms. Fig. 6 also includes the CDFs of the exact PL computation time, which is significantly longer than the overestimation method and heavily influenced by fault type: approximately 0.1 seconds for NLoS faults and several seconds for clock faults. This discrepancy is due to the weights of GM posterior PDFs (29): with the NLoS-type faults, only a few terms have significant weights, while with the clock-type faults, no term tends to dominate. As a result, the choice of $\zeta_2 = 0.002$ (see (40)) typically reduces the GM model to less than 10 terms for NLoS-type fault, but several hundred terms for the clock-type case. Further studies show that even with $\zeta_2 = 0.1$, around a hundred terms can still remain.

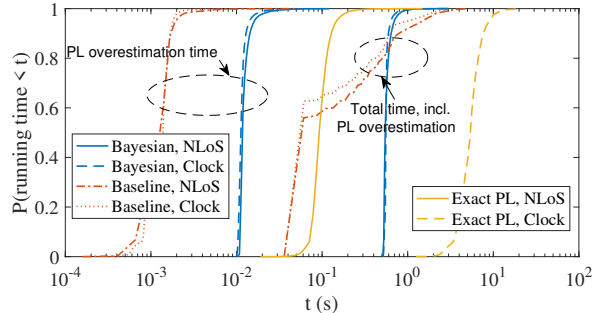


Fig. 6. Empirical CDF of running times, including the total and PL computation times for Baseline RAIM and Bayesian RAIM with PL overestimation, along with the running time for Algorithm 1.

TABLE II

BAYESIAN RAIM PERFORMANCE WITH INITIAL POSITIONING ERRORS: (1) 45°-DIRECTION + NLOS-FAULT, (2) 45°-DIRECTION + CLOCK-FAULT, (3) V-DIRECTION + NLOS-FAULT, (4) V-DIRECTION + CLOCK-FAULT.

		PL@50% [m]			Simulated IR [$\times 10^{-3}$]		
		min	max	CV	min	max	CV
E_H	1	0.71	0.71	0.01%	0.94	1.0	1.6%
	2	0.73	0.73	0.02%	0.87	0.96	2.4%
	3	7.32	7.52	0.96%	0.96	1.1	3.3%
	4	34.0	34.1	0.06%	0.78	0.95	5.9%
E_V	1	0.70	0.74	1.8%	0.84	1.1	7.5%
	2	0.72	0.76	1.4%	0.87	1.0	4.5%
	3	5.31	11.04	25.7%	0.94	5.4	77.0%
	4	16.7	47.6	34.6%	0.76	1.2	13.2%

TABLE III

BASELINE RAIM PERFORMANCE WITH INITIAL POSITIONING ERRORS: (1) H-PLANE + NLOS-FAULT, (2) H-PLANE + CLOCK-FAULT, (3) V-DIRECTION + NLOS-FAULT, (4) V-DIRECTION + CLOCK-FAULT.

		PL@50% [m]			Simulated IR [$\times 10^{-5}$]		
		min	max	CV	min	max	CV
E_H	1	2.31	2.34	0.38%	4.4	4.6	2.3%
	2	2.31	2.33	0.35%	2.4	2.8	5.9%
	3	105.5	106.5	0.32%	1.6	1.8	5.3%
	4	105.5	106.4	0.27%	1.8	2.6	13.7%
E_V	1	2.20	2.35	2.4%	1.8	5.8	31.3%
	2	2.20	2.35	2.4%	2.6	4.6	17.1%
	3	55.5	148.4	33.6%	0.4	3.8	54.5%
	4	55.5	148.3	33.6%	2.0	3.4	22.5%

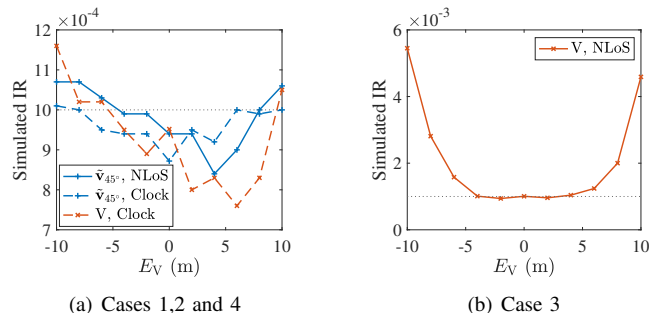


Fig. 7. Simulated IR performance of Bayesian RAIM with vertical initial positioning error.

C. Performance Sensitivity Study Results

We evaluate the sensitivity of the algorithms to initial positioning errors using the 50th percentile PL and the simulated IR. As the results turn show relative insensitivity as E_H varying in the $[0, 5]$ m range and E_V in $[-10, 10]$ m range, we show them as tables as opposed to plots. Specifically, Table II presents their minimum, maximum, and coefficient of variation

(CV, defined as the ratio of the standard deviation to the mean) for Bayesian RAIM, while Table III provides these metrics for Baseline RAIM.

1) *Bayesian RAIM*: As Table II shows, the horizontal initial positioning error E_H has minimal effect on the 50th percentile PL for both the H-plane (cases 1-2) and the V-direction (cases 3-4). However, it can cause the maximum simulated IR (case 3) to exceed the TIR requirement. In contrast, the vertical initial positioning error E_V significantly affects these metrics, especially in the V-direction. Under NLoS fault conditions, the simulated IR in the V-direction (case 3) exceeds five times the TIR. Fig. 7 displays the curves of the simulated IR over E_V , showing that the IR increases with $|E_V|$. No clear trends were observed for other metrics, so they are not included here.

2) *Baseline RAIM*: Table III shows that initial positioning errors similarly affect the performance of Baseline RAIM. However, because it computes much looser PLs, the simulated IRs remain in the order of 10^{-5} . Additionally, the 50th percentile PL values under both NLoS and Clock-type faults are almost identical, indicating the insensitivity of Baseline RAIM to the fault distribution. This contrasts with the Bayesian RAIM, which exhibits sensitivity to fault distribution.

3) *Discussion and Implications*: Bayesian RAIM computes the exact posterior PDFs of the UE's position based on the linear measurement model (2) and the distributions of bias and noise, making it sensitive to model mismatches. Due to the relative low heights of the BS, the already small third entry of $\mathbf{g}_i = (\mathbf{x}_{u,0} - \mathbf{x}_i) / \|\mathbf{x}_{u,0} - \mathbf{x}_i\| \approx (\mathbf{x}_u - \mathbf{x}_i + \mathbf{e}_{0,V}) / \|\mathbf{x}_u - \mathbf{x}_i\|$, is significantly affected by high vertical error magnitude $|E_V|$. With an average BS height of just 19.2 meters in our simulation, a maximum $|E_V|$ value of 10 meters can cause a substantial error in the unit vector. The results reaffirm that effective positioning performance, including robust integrity assurance, critically hinges on the geometric placement of BSs. Additionally, investigating methods to incorporate potential model errors into the problem formulation emerges as a promising direction for future research.

VII. CONCLUSIONS

In this paper, we developed a Bayesian RAIM algorithm for ToA-based, snapshot-type 3D cellular positioning to address measurement faults. This algorithm computes the posterior PDF of the UE position via message passing along a factor graph, leveraging the joint probability of the UE position and measurement states based on a linearized measurement model. To enable efficient message passing, we derived computational rules for Gaussian messages that ensure accurate scaling factor calculations and effectively manage degenerate Gaussian densities. The resulting posterior PDF fully incorporates all relevant measurement information, eliminating the need to discard any measurements, and enables the computation of exact 1D PLs in any direction within \mathbb{R}^3 at low computational cost. This also facilitates the immediate calculation of 2D or 3D PLs overestimates. Additionally, we developed an exact 2D/3D PL search algorithm by translating the probability of a Gaussian-distributed random vector within an ellipsoid into the CDF of a generalized chi-squared random variable.

For performance evaluation, we adapted an advanced RAIM algorithm [14] to the same problem setting and used it as a baseline in our numerical studies. Monte-Carlo simulations shown that our proposed Bayesian RAIM algorithm achieves tighter PLs with over 50% reduction in all the evaluated cases (Table I) compared to the baseline algorithm, even when using the low-complexity PL overestimation method. It closely meets the TIR requirement with the exact PL computations. Furthermore, the simulated results highlights the importance of a good BS distribution condition. Under such condition, the Bayesian RAIM demonstrates robustness against errors in initial position estimates where model linearization occurs, making it both effective and reliable for enhancing positioning integrity in 3D cellular environments.

APPENDIX A PROOF OF LEMMA 1

Lemma 1 follows since

$$\begin{aligned} \Pr \{ \|\mathbf{e}_{nD}\| > \text{PL}_{nD}^U \} &\stackrel{(a)}{\leq} \Pr \{ \cup_{i=1}^n |e_i| > \text{PL}_{1D,i} \} \\ &\stackrel{(b)}{\leq} \sum_{i=1}^n \Pr \{ |e_i| > \text{PL}_{1D,i} \} \stackrel{(c)}{<} \sum_{i=1}^n w_i P_{\text{TIR}} = P_{\text{TIR}}. \end{aligned}$$

The inequality (a) can be verified from geometry: $\cup_{i=1}^n |e_i| > \text{PL}_{1D,i}$ describes the event when the error vector \mathbf{e}_{nD} is located outside the 2D/3D box with edge lengths given by $\{2\text{PL}_{1D,i}\}$; while $\|\mathbf{e}_{nD}\| > \text{PL}_{nD}^U$ is the event when \mathbf{e}_{nD} is located outside the 2D circle/3D sphere with radius PL_{nD}^U , which encloses the box. The inequality (b) follows the union bound, and (c) follows from the assumption (5).

APPENDIX B MESSAGE PASSING RULES FOR PROBLEM 1

A. General Gaussian Distribution

A rigorous definition of a general Gaussian random vector, following [32, Definition 23.1.1], is given below. An equivalent definition can be found in [33, Definition 2.1].

Definition 2 (Gaussian Random Vector). A real random vector $\mathbf{X} = (X_1, \dots, X_n)^T$ is said to be Gaussian if there exists a deterministic matrix $\mathbf{A} \in \mathbb{R}^{n \times m}$ and a deterministic vector $\mathbf{m} \in \mathbb{R}^n$ such that the distribution of \mathbf{X} is equal to that of $\mathbf{AZ} + \mathbf{m}$, where \mathbf{Z} is a standard Gaussian vector with m components. The distribution is denoted by $\mathbf{X} \sim \mathcal{N}(\mathbf{x}; \mathbf{m}, \Sigma)$, where $\Sigma \triangleq \mathbf{AA}^T \succeq 0$ is the covariance matrix. The PDF of \mathbf{X} is given by

$$f_{\mathbf{X}}(\mathbf{x}) = \frac{\exp \left[-\frac{1}{2}(\mathbf{x} - \mathbf{m})^T \Sigma^+ (\mathbf{x} - \mathbf{m}) \right]}{(2\pi)^{k/2} |\Sigma|_+^{1/2}}, \quad (43)$$

where $k = \text{rank}(\Sigma)$, and Σ^+ and $|\Sigma|_+$ are the pseudo-inverse⁸ and pseudo-determinant⁹ of Σ , respectively.

In this definition, n can be greater than, equal to, or smaller than m ; $k \leq \min(m, n)$. When $\Sigma \succ 0$, Σ^+ and $|\Sigma|_+$ coincide

⁸The pseudo-inverse (Moore–Penrose inverse) of \mathbf{A} is the matrix \mathbf{A}^+ that satisfies [30, Section 3.6]: (i) $\mathbf{AA}^+\mathbf{A} = \mathbf{A}$; (ii) $\mathbf{A}^+\mathbf{AA}^+ = \mathbf{A}^+$; (iii) \mathbf{AA}^+ is symmetric; (iv) $\mathbf{A}^+\mathbf{A}$ is symmetric. The pseudo-inverse is unique and always exists, with $(\mathbf{A}^+)^+ = \mathbf{A}$. When \mathbf{A} has full-rank, it has explicit expressions: for full row rank, $\mathbf{A}^+ = \mathbf{A}^T(\mathbf{AA}^T)^{-1}$; for full column rank, $\mathbf{A}^+ = (\mathbf{A}^T\mathbf{A})^{-1}\mathbf{A}^T$.

⁹The pseudo-determinant of $\Sigma \succeq 0$ is given by $|\Sigma|_+ \triangleq \prod_{i=1}^k \gamma_i^+$, where $\gamma_1^+, \dots, \gamma_k^+$ are the positive eigenvalues of Σ .

with the regular inverse Σ^{-1} and determinant $|\Sigma|$. Expanding (43), we have

$$f_{\mathbf{X}}(\mathbf{x}) = \frac{\exp\left(-\frac{1}{2}\mathbf{x}^T\Sigma^+\mathbf{x} + \mathbf{x}^T\Sigma^+\mathbf{m} - \frac{1}{2}\mathbf{m}^T\Sigma^+\mathbf{m}\right)}{(2\pi)^{k/2}|\Sigma|_+^{1/2}} \quad (44)$$

$$= \frac{|\mathbf{V}|_+^{1/2} \exp\left(-\frac{1}{2}\mathbf{x}^T\mathbf{V}\mathbf{x} + \mathbf{x}^T\mathbf{u} - \frac{1}{2}\mathbf{u}^T\mathbf{V}^+\mathbf{u}\right)}{(2\pi)^{k/2}}, \quad (45)$$

where $\mathbf{V} \triangleq \Sigma^+$, $\mathbf{u} \triangleq \mathbf{V}\mathbf{m}$, and it can be easily verified that $\mathbf{m}^T\Sigma^+\mathbf{m} = \mathbf{u}^T\mathbf{V}^+\mathbf{u}$. This demonstrates that the Gaussian distribution can be equivalently parameterized using (\mathbf{m}, Σ) or (\mathbf{u}, \mathbf{V}) . Note that $\text{rank}(\Sigma) = \text{rank}(\mathbf{V})$. To avoid ambiguity, we denote the PDF expression in (43) by $f_{\mathbf{X}}(\mathbf{x}; \mathbf{m}, \Sigma)$ and in (45) by $f_{\mathbf{X}}^{\text{E}}(\mathbf{x}; \mathbf{u}, \mathbf{V})$. Finally, recall $\alpha_{\mathbf{X}} \triangleq -\frac{1}{2}\mathbf{m}^T\Sigma^+\mathbf{m} \equiv -\frac{1}{2}\mathbf{u}^T\mathbf{V}^+\mathbf{u}$, as defined in (16).

B. Proof of Lemma 2

Consider $\mathbf{u}_{\mathbf{X}}$ and $\mathbf{V}_{\mathbf{X}}$ given in (17b). Since $\mathbf{A} \in \mathbb{R}^{m \times n}$ has full row rank, we have $\text{rank}(\mathbf{V}_{\mathbf{X}}) = \text{rank}(\mathbf{V}_{\mathbf{Y}}) = m$ and $\mathbf{A}\mathbf{A}^+ = \mathbf{I}_m$. Therefore $\mathbf{u}_{\mathbf{X}}^T\mathbf{V}_{\mathbf{X}}^+\mathbf{u}_{\mathbf{X}} = \mathbf{u}_{\mathbf{Y}}^T\mathbf{A}\mathbf{A}^+\mathbf{V}_{\mathbf{Y}}^+(\mathbf{A}\mathbf{A}^+)^T\mathbf{u}_{\mathbf{Y}} = \mathbf{u}_{\mathbf{Y}}^T\mathbf{V}_{\mathbf{Y}}^+\mathbf{u}_{\mathbf{Y}}$, where the property $(\mathbf{A}\mathbf{B})^+ = \mathbf{B}^+\mathbf{A}^+$ is used. Thus, $\alpha_{\mathbf{X}} = \alpha_{\mathbf{Y}}$. Given this, we confirms the correctness of (17a)–(17c):

$$\begin{aligned} & f_{\mathbf{Y}}^{\text{E}}(\mathbf{A}\mathbf{x}; \mathbf{u}_{\mathbf{Y}}, \mathbf{V}_{\mathbf{Y}}) \\ &= \frac{|\mathbf{V}_{\mathbf{Y}}|_+^{1/2}}{(2\pi)^{m/2}} \exp\left[-\frac{1}{2}(\mathbf{A}\mathbf{x})^T\mathbf{V}_{\mathbf{Y}}\mathbf{A}\mathbf{x} + (\mathbf{A}\mathbf{x})^T\mathbf{u}_{\mathbf{Y}} + \alpha_{\mathbf{Y}}\right] \\ &= \underbrace{\frac{|\mathbf{V}_{\mathbf{Y}}|_+^{1/2}}{|\mathbf{V}_{\mathbf{X}}|_+^{1/2}}}_{s_{\mathbf{Y}}^{\mathbf{X}}} \underbrace{\frac{|\mathbf{V}_{\mathbf{X}}|_+^{1/2}}{(2\pi)^{m/2}} \exp\left(-\frac{1}{2}\mathbf{x}^T\mathbf{V}_{\mathbf{X}}\mathbf{x} + \mathbf{x}^T\mathbf{u}_{\mathbf{X}} + \alpha_{\mathbf{X}}\right)}_{f_{\mathbf{X}}^{\text{E}}(\mathbf{x}; \mathbf{u}_{\mathbf{X}}, \mathbf{V}_{\mathbf{X}})}. \end{aligned}$$

C. Proof of Lemma 3

The following lemma is need for the proof of Lemma 3. It provides the computation rule for the product of two arbitrary, possibly degenerate, Gaussian densities.

Lemma 4 (Product of two Gaussian densities). *Given two messages of \mathbf{X} in the form of Gaussian densities: $\mu_{\mathbf{X},1}(\mathbf{x}) = f_{\mathbf{X}}^{\text{E}}(\mathbf{x}; \mathbf{u}_{\mathbf{X}_1}, \mathbf{V}_{\mathbf{X}_1})$ and $\mu_{\mathbf{X},2}(\mathbf{x}) = f_{\mathbf{X}}^{\text{E}}(\mathbf{x}; \mathbf{u}_{\mathbf{X}_2}, \mathbf{V}_{\mathbf{X}_2})$, where $\text{rank}(\mathbf{V}_{\mathbf{X}_1}) = k_1$ and $\text{rank}(\mathbf{V}_{\mathbf{X}_2}) = k_2$, their product is given by*

$$f_{\mathbf{X}}^{\text{E}}(\mathbf{x}; \mathbf{u}_{\mathbf{X}_1}, \mathbf{V}_{\mathbf{X}_1}) f_{\mathbf{X}}^{\text{E}}(\mathbf{x}; \mathbf{u}_{\mathbf{X}_2}, \mathbf{V}_{\mathbf{X}_2}) = s_{\mathbf{X}_{1:2}} f_{\mathbf{X}}^{\text{E}}(\mathbf{x}; \mathbf{u}_{\mathbf{X}}, \mathbf{V}_{\mathbf{X}}), \quad (46a)$$

where $\mathbf{u}_{\mathbf{X}} = \mathbf{u}_{\mathbf{X}_1} + \mathbf{u}_{\mathbf{X}_2}$ and $\mathbf{V}_{\mathbf{X}} = \mathbf{V}_{\mathbf{X}_1} + \mathbf{V}_{\mathbf{X}_2}$, and the scaling factor $s_{\mathbf{X}_{1:2}}$ is given by ($k = \text{rank}(\mathbf{V}_{\mathbf{X}})$)

$$s_{\mathbf{X}_{1:2}} = \frac{|\mathbf{V}_{\mathbf{X}_1}|_+^{1/2} |\mathbf{V}_{\mathbf{X}_2}|_+^{1/2}}{(2\pi)^{(k_1+k_2-k)/2} |\mathbf{V}_{\mathbf{X}}|_+^{1/2}} \exp(\alpha_{\mathbf{X}_1} + \alpha_{\mathbf{X}_2} - \alpha_{\mathbf{X}}). \quad (46b)$$

Proof. Using the PDF expression (45), we immediately have

$$\begin{aligned} & f_{\mathbf{X}}^{\text{E}}(\mathbf{x}; \mathbf{u}_{\mathbf{X}_1}, \mathbf{V}_{\mathbf{X}_1}) f_{\mathbf{X}}^{\text{E}}(\mathbf{x}; \mathbf{u}_{\mathbf{X}_2}, \mathbf{V}_{\mathbf{X}_2}) = \frac{|\mathbf{V}_{\mathbf{X}_1}|_+^{1/2} |\mathbf{V}_{\mathbf{X}_2}|_+^{1/2}}{(2\pi)^{k_1/2} (2\pi)^{k_2/2}} \\ & \exp\left[-\frac{1}{2}\mathbf{x}^T(\mathbf{V}_{\mathbf{X}_1} + \mathbf{V}_{\mathbf{X}_2})\mathbf{x} + \mathbf{x}^T(\mathbf{u}_{\mathbf{X}_1} + \mathbf{u}_{\mathbf{X}_2}) + \alpha_{\mathbf{X}_1} + \alpha_{\mathbf{X}_2}\right] \\ &= \underbrace{\frac{|\mathbf{V}_{\mathbf{X}_1}|_+^{1/2} |\mathbf{V}_{\mathbf{X}_2}|_+^{1/2}}{(2\pi)^{(k_1+k_1-k)/2} |\mathbf{V}_{\mathbf{X}}|_+^{1/2}}}_{s_{\mathbf{X}_{1:2}}} \exp(\alpha_{\mathbf{X}_1} + \alpha_{\mathbf{X}_2} - \alpha_{\mathbf{X}}). \end{aligned}$$

$$\frac{|\mathbf{V}_{\mathbf{X}}|_+^{1/2}}{(2\pi)^{k/2}} \exp\left(-\frac{1}{2}\mathbf{x}^T\mathbf{V}_{\mathbf{X}}\mathbf{x} + \mathbf{x}^T\mathbf{u}_{\mathbf{X}} + \alpha_{\mathbf{X}}\right) = \underbrace{f_{\mathbf{X}}^{\text{E}}(\mathbf{x}; \mathbf{u}_{\mathbf{X}}, \mathbf{V}_{\mathbf{X}})}_{f_{\mathbf{X}}^{\text{E}}(\mathbf{x}; \mathbf{u}_{\mathbf{X}}, \mathbf{V}_{\mathbf{X}})}$$

If $\mathbf{V}_{\mathbf{X}_1} \succ 0$ and $\mathbf{V}_{\mathbf{X}_2} \succ 0$, (46a)–(46b) can be obtained by using [30, Eq. (358)–Eq. (364)]. \square

Based Lemma 4, the computation rule for the product of multiple Gaussian densities in Lemma 3 can be verified by successively performing the product of two Gaussian densities.

APPENDIX C

PROOF OF THEOREM 1

We first show that the probability of a Gaussian distributed vector in \mathbb{R}^N lying within an arbitrary ellipsoid in \mathbb{R}^N can be calculated by computing the CDF of a generalized chi-squared random variable. An ellipsoid in \mathbb{R}^N centered at $\mathbf{c} \in \mathbb{R}^N$ is defined as $\mathcal{E}(\mathbf{A}, \mathbf{c}, \rho) = \{\mathbf{x} \in \mathbb{R}^N : (\mathbf{x} - \mathbf{c})^T \mathbf{A} (\mathbf{x} - \mathbf{c}) \leq \rho\}$, where $\mathbf{A} \in \mathbb{R}^{N \times N}$ is symmetric positive definite, and ρ is a positive real value. The eigendecomposition of \mathbf{A} is $\mathbf{A} = \mathbf{Q}\mathbf{D}\mathbf{Q}^T$, where $\mathbf{D} = \text{diag}(d_1, \dots, d_N)$ and $\mathbf{Q} \in \mathbb{R}^{N \times N}$ is orthogonal. The lengths of the N semi-axes are given by $\rho/\sqrt{d_1}, \dots, \rho/\sqrt{d_N}$. Consider a random vector $\mathbf{X} \in \mathbb{R}^N$ that follows a Gaussian distribution $\mathcal{N}(\mathbf{x}; \mathbf{m}, \Sigma)$ where $\Sigma \succ 0$. Let $Z = (\mathbf{X} - \mathbf{c})^T \mathbf{A} (\mathbf{X} - \mathbf{c})$. The probability of \mathbf{X} lying within $\mathcal{E}(\mathbf{A}, \mathbf{c}, \rho)$ is

$$\int_{\mathcal{E}(\mathbf{A}, \mathbf{c}, \rho)} f_{\mathbf{X}}(\mathbf{x}; \mathbf{m}, \Sigma) d\mathbf{x} = F_Z(\rho), \quad (47)$$

where $F_Z(z) \triangleq \Pr(Z \leq z)$ is the CDF of Z . We will show that Z is a generalized chi-squared random variable determined by $\mathbf{m}, \Sigma, \mathbf{A}, \mathbf{c}$.

Given $\mathbf{A} \succ 0$ and $\Sigma \succ 0$, we have

$$\Sigma^{\frac{1}{2}} \mathbf{A} \Sigma^{\frac{1}{2}} = \mathbf{P}\Omega\mathbf{P}^T, \quad (48)$$

where $\Omega = \text{diag}(\omega_1, \dots, \omega_N)$ with $\omega_i > 0$, and $\mathbf{P} \in \mathbb{R}^{N \times N}$ is orthogonal. It can be shown that $\mathbf{Y} = \mathbf{P}^T \Sigma^{-\frac{1}{2}} (\mathbf{X} - \mathbf{c}) \sim \mathcal{N}(\mathbf{y}; \boldsymbol{\nu}, \mathbf{I}_N)$, where

$$\boldsymbol{\nu} \triangleq \mathbf{P}^T \Sigma^{-\frac{1}{2}} (\mathbf{m} - \mathbf{c}). \quad (49)$$

Letting Y_i be the i -th element of \mathbf{Y} and ν_i be the i -th entry of $\boldsymbol{\nu}$. Then Y_i^2 follows a noncentral chi-square distribution with one degree of freedom and noncentrality parameter ν_i^2 (i.e., $Y_i^2 \sim \chi^2(1, \nu_i^2)$). We can rewrite Z as

$$Z = \mathbf{Y}^T \Omega \mathbf{Y} = \sum_{i=1}^N \omega_i Y_i^2. \quad (50)$$

This shows that Z is a weighted sum of N independent non-central chi-square random variables. Summarizing the above, we have the following lemma.

Lemma 5. *The probability that a Gaussian random vector $\mathbf{X} \in \mathbb{R}^N \sim \mathcal{N}(\mathbf{x}; \mathbf{m}, \Sigma)$ lies within an ellipsoid $\mathcal{E}(\mathbf{A}, \mathbf{c}, \rho) \in \mathbb{R}^N$ is given by $F_Z(\rho)$, the CDF of a generalized chi-squared random variable Z evaluated at ρ . Specifically, $Z = \sum_{i=1}^N \omega_i W_i$ where $W_i \sim \chi^2(1, \nu_i^2)$, $i = 1, \dots, N$, and the weights $\{\omega_i\}$ and noncentrality parameters $\{\nu_i^2\}$ are determined by $\mathbf{m}, \Sigma, \mathbf{A}, \mathbf{c}$ via (48) and (49).*

By setting $\mathbf{A} = \mathbf{I}_n$, $\mathbf{c} = \mathbf{0}$, and $\rho = r^2$, the ellipsoid $\mathcal{E}(\mathbf{A}, \mathbf{c}, \rho)$ becomes a circle (for $n = 2$) or a sphere (for $n = 3$) centered at the origin with radius r . Using the PDFs

of e_{nD} given by (30) and (32), the probability that e_{nD} lies within a circle/sphere of radius r is $\Pr \{e_{nD} \in \mathcal{E}(l_n, \mathbf{0}, r^2)\} = \sum_{i=1}^L w_{\mathbf{X}}^{(i)} F_{Z_i}(r^2)$, where $F_{Z_i}(r^2)$ is the CDF of the generalized chi-squared random variable Z_i given by (36) computed at r^2 . With this, the proof of Theorem 1 follows directly from Lemma 5.

APPENDIX D

NUMERICAL COMPUTATION METHOD FOR THE CDF OF A GENERALIZED CHI-SQUARED RANDOM VARIABLE

There is no closed-form expression for the PDF, CDF, and inverse CDF of a generalized chi-squared variable $Z = \sum_{i=1}^N \omega_i W_i$, for $W_i \sim \chi^2(k_i, \theta_i)$, where $\chi^2(k_i, \theta_i)$ denotes a noncentral chi-square distribution with k_i degrees of freedom and noncentral parameter θ_i . (Setting $k_i = 1$ and $\theta_i = \nu_i^2$ yields (50).) Numerical methods can be used instead. The Imhof method computes $F_Z(z)$, the CDF of Z , as a numerical integral $F_Z(z) \approx \frac{1}{2} - \frac{1}{\pi} \int_0^U \frac{\sin \beta(u, z)}{u \kappa(u)} du$, where

$$\beta(u, z) = \frac{1}{2} \sum_{i=1}^N \left(k_i \arctan \omega_i u + \frac{\theta_i \omega_i u}{1 + \omega_i^2 u^2} \right) - \frac{1}{2} z u, \quad (51a)$$

$$\kappa(u) = \exp \left(\frac{1}{4} \sum_{i=1}^N k_i \ln(1 + \omega_i^2 u^2) + \frac{1}{2} \sum_{i=1}^N \frac{\theta_i \omega_i^2 u^2}{1 + \omega_i^2 u^2} \right). \quad (51b)$$

The error for terminating at U is given by $\xi(U) = \frac{1}{\pi} \int_U^\infty \frac{\sin \beta(u, y)}{u \kappa(u)} du$. It is shown in [34] that $|\xi(U)| \leq \Xi(U)$, where

$$\Xi(U) = \left[\pi K U^K \prod_{i=1}^N |\omega_i|^{\frac{k_i}{2}} \exp \left(\frac{1}{2} \sum_{i=1}^n \frac{\theta_i \omega_i^2 U^2}{1 + \omega_i^2 U^2} \right) \right]^{-1} \quad (52)$$

with $K = \frac{1}{2} \sum_{i=1}^N k_i$. Thus, for any required accuracy ϵ , a sufficiently large U can be found to ensure $\Xi(U) \leq \epsilon$.

REFERENCES

- [1] L. Ding, G. Seco-Granados, H. Kim, R. Whiton, E. G. Ström, J. Sjöberg, and H. Wymeersch, "Bayesian integrity monitoring for cellular positioning — a simplified case study," in *IEEE ICC Workshops*, 2023, pp. 1050–1056.
- [2] C. De Lima, D. Belot, R. Berkvens, A. Bourdoux, D. Dardari, M. Guillaud, M. Isomursu, E.-S. Lohan, Y. Miao, A. N. Barreto *et al.*, "Convergent communication, sensing and localization in 6G systems: An overview of technologies, opportunities and challenges," *IEEE Access*, vol. 9, pp. 26902–26925, 2021.
- [3] A. Behravan, V. Yajnanarayana, M. F. Keskin, H. Chen, D. Shrestha, T. E. Abrudan, T. Svensson, K. Schindhelm, A. Wolfgang, S. Lindberg *et al.*, "Positioning and sensing in 6G: Gaps, challenges, and opportunities," *IEEE Veh. Technol. Mag.*, vol. 18, no. 1, pp. 40–48, 2022.
- [4] R. Whiton, "Cellular localization for autonomous driving: A function pull approach to safety-critical wireless localization," *IEEE Veh. Technol. Mag.*, vol. 17, no. 4, pp. 2–11, 2022.
- [5] S. Bartoletti, H. Wymeersch, T. Mach, O. Brunnegård, D. Giustiniano, P. Hammarberg, M. F. Keskin, J. O. Lacruz, S. M. Razavi, J. Rönnblom *et al.*, "Positioning and sensing for vehicular safety applications in 5G and beyond," *IEEE Commun. Mag.*, vol. 59, no. 11, pp. 15–21, 2021.
- [6] N. Zhu, J. Marais, D. Betaille, and M. Berbineau, "GNSS position integrity in urban environments: A review of literature," *IEEE Trans. Intell. Transp. Syst.*, vol. 19, no. 9, pp. 2762–2778, 2018.
- [7] 3GPP, "Study on expanded and improved NR positioning," 3rd Generation Partnership Project (3GPP), Technical Report (TR) 38.859, Dec 2022, version 18.0.0.
- [8] P. Hammarberg, J. Vinogradova, G. Fodor, R. Shreevastav, S. Dwivedi, and F. Gunnarsson, "Architecture, protocols, and algorithms for location-aware services in beyond 5G networks," *IEEE Commun. Stand. Mag.*, vol. 6, no. 4, pp. 88–95, 2022.
- [9] H. Jing, Y. Gao, S. Shahbeigi, and M. Dianati, "Integrity monitoring of GNSS/INS based positioning systems for autonomous vehicles: State-of-the-art and open challenges," *IEEE Trans. Intell. Transp. Syst.*, vol. 23, no. 9, pp. 14166–14187, 2022.
- [10] B. W. Parkinson and P. Axelrad, "Autonomous GPS integrity monitoring using the pseudorange residual," *Navigation*, vol. 35, no. 2, pp. 255–274, 1988.
- [11] R. G. Brown, "Receiver autonomous integrity monitoring," *Global Positioning System: Theory and applications.*, vol. 2, pp. 143–165, 1996.
- [12] G. Schroth, A. Ene, J. Blanch, T. Walter, and P. Enge, "Failure detection and exclusion via range consensus," in *Eur. Navig. Conf.*, 2008.
- [13] G. Castaldo, A. Angrisano, S. Gaglione, and S. Troisi, "P-RANSAC: An integrity monitoring approach for GNSS signal degraded scenario," *Int. J. Navig. Obs.*, 2014.
- [14] J. Blanch, T. Walker, P. Enge, Y. Lee, B. Pervan, M. Rippl, A. Spletter, and V. Kropp, "Baseline advanced RAIM user algorithm and possible improvements," *IEEE Trans. Aerosp. Electron. Syst.*, vol. 51, no. 1, pp. 713–732, 2015.
- [15] P. Zabalegui, G. De Miguel, A. Pérez, J. Mendizabal, J. Goya, and I. Adin, "A review of the evolution of the integrity methods applied in GNSS," *IEEE Access*, vol. 8, pp. 45813–45824, 2020.
- [16] M. Joergler and B. Pervan, "Kalman filter-based integrity monitoring against sensor faults," *Journal of Guidance, Control, and Dynamics*, vol. 36, no. 2, pp. 349–361, 2013.
- [17] M. Maaref and Z. M. Kassas, "Autonomous integrity monitoring for vehicular navigation with cellular signals of opportunity and an IMU," *IEEE Trans. Intell. Transp. Syst.*, vol. 23, no. 6, pp. 5586–5601, 2021.
- [18] Y. Sun, L. Cao, S. Li, and Z. Deng, "G5GIM: Integrity monitoring for GNSS/5G integrated navigation of urban vehicles," *IEEE Trans. Instrum. Meas.*, 2023.
- [19] P. Ober, "Integrity according to Bayes," in *IEEE Position Location and Navigation Symposium*. IEEE, 2000, pp. 325–332.
- [20] H. Pesonen, "A framework for Bayesian receiver autonomous integrity monitoring in urban navigation," *Navigation*, vol. 58, no. 3, pp. 229–240, 2011.
- [21] S. Gupta and G. X. Gao, "Particle RAIM for integrity monitoring," in *Proc. 32nd ION GNSS*, 2019, pp. 811–826.
- [22] J. Gabela, A. Kealy, M. Hedley, and B. Moran, "Case study of Bayesian RAIM algorithm integrated with spatial feature constraint and fault detection and exclusion algorithms for multi-sensor positioning," *Navigation*, vol. 68, no. 2, pp. 333–351, 2021.
- [23] Q. Zhang and Q. Gui, "A new Bayesian RAIM for multiple faults detection and exclusion in GNSS," *J. Navig.*, vol. 68, no. 3, pp. 465–479, 2015.
- [24] H.-A. Loeliger, "An introduction to factor graphs," *IEEE Signal Processing Magazine*, vol. 21, no. 1, pp. 28–41, 2004.
- [25] H.-A. Loeliger, J. Dauwels, J. Hu, S. Korl, L. Ping, and F. R. Kschischang, "The factor graph approach to model-based signal processing," *Proc. IEEE*, vol. 95, no. 6, pp. 1295–1322, 2007.
- [26] M. Koivisto, M. Costa, J. Werner *et al.*, "Joint device positioning and clock synchronization in 5G ultra-dense networks," *IEEE Trans. Wirel. Commun.*, vol. 16, no. 5, pp. 2866–2881, 2017.
- [27] I. Guvenc, S. Gezici, and Z. Sahinoglu, "Fundamental limits and improved algorithms for linear least-squares wireless position estimation," *Wirel. Commun. Mob. Comput.*, vol. 12, no. 12, pp. 1037–1052, 2012.
- [28] S. Zhu and Z. Ding, "A simple approach of range-based positioning with low computational complexity," *IEEE Trans. Wirel. Commun.*, vol. 8, no. 12, pp. 5832–5836, 2009.
- [29] F. R. Kschischang, B. J. Frey, and H.-A. Loeliger, "Factor graphs and the sum-product algorithm," *IEEE Trans. Inf. Theory*, vol. 47, no. 2, pp. 498–519, 2001.
- [30] K. B. Petersen, M. S. Pedersen *et al.*, "The matrix cookbook," *Technical University of Denmark*, vol. 7, no. 15, p. 510, 2008.
- [31] D. A. Bodenham and N. M. Adams, "A comparison of efficient approximations for a weighted sum of chi-squared random variables," *Stat. Comput.*, vol. 26, no. 4, pp. 917–928, 2016.
- [32] A. Lapidoth, *A Foundation in Digital Communication*. Cambridge University Press, 2017.
- [33] V. A. Nguyen, D. Kuhn, and P. Mohajerin Esfahani, "Distributionally robust inverse covariance estimation: The Wasserstein shrinkage estimator," *Operations research*, vol. 70, no. 1, pp. 490–515, 2022.
- [34] J.-P. Imhof, "Computing the distribution of quadratic forms in normal variables," *Biometrika*, vol. 48, no. 3/4, pp. 419–426, 1961.